Optimizing Sensitive Weight Configurations on a Fast-Planing Vessel to Reduce Drag

Muhammad Luqman Hakim
Department of Naval Architecture, Faculty of Engineering, Universitas Diponegoro

Purnamasari, Dian
Research Center for Hydrodynamics Technology, National Research and Innovation Agency (BRIN)

Mohammad, Luthfansyah
Automation Engineering Technology Study Program, Vocational School, Universitas Diponegoro

Patricia Evericho Mountaines
Department of Computer Engineering, Faculty of Engineering, Universitas Diponegoro

他

https://doi.org/10.5109/7236842

出版情報：Evergreen. 11 (3), pp.1919-1939, 2024-09. 九州大学グリーンテクノロジー研究教育センター
バージョン：

EVERGREEN Joint Journal of Novel Carbon Resource Sciences & Green Asia Strategy, Vol. 11, Issue 03, pp1919-1939, September, 2024

Optimizing Sensitive Weight Configurations on a Fast-Planing Vessel to Reduce Drag

Muhammad Luqman Hakim[1,*], Dian Purnamasari[2], Luthfansyah Mohammad[3], Patricia Evericho Mountaines[4], Diva Kurnianingtyas[5], Dendy Satrio[6], Muhammad Hafiz Nurwahyu Aliffrananda[7]

[1]Department of Naval Architecture, Faculty of Engineering, Universitas Diponegoro, Semarang 50275, Indonesia

[2]Research Center for Hydrodynamics Technology, National Research and Innovation Agency (BRIN), Surabaya 60117, Indonesia

[3]Automation Engineering Technology Study Program, Vocational School, Universitas Diponegoro, Semarang 50275, Indonesia

[4]Department of Computer Engineering, Faculty of Engineering, Universitas Diponegoro, Semarang 50275, Indonesia

[5]Department of Informatics Engineering, Faculty of Computer Science, Universitas Brawijaya, Malang 65145, Indonesia

[6]Department of Ocean Engineering, Institut Teknologi Sepuluh Nopember, Surabaya 60111, Indonesia

[7]Department of Mechanical Engineering, Faculty of Engineering, University of Melbourne, Victoria 3010, Australia

*Author to whom correspondence should be addressed:
E-mail: mluqmanhak@lecturer.undip.ac.id

(Received December 12, 2023; Revised August 5, 2024; Accepted August 30, 2024).

Abstract: In the realm of high-speed planing crafts, characterized by their diminutive size, an acute sensitivity to variations in weight and center of gravity is observed. This investigation delves into the consequential influence of alterations in weight and center of gravity on the resistance encountered by these crafts. The primary goal is to scrutinize a methodology aimed at optimizing weight and center of gravity for small, high-speed planing crafts, with the explicit aim of minimizing drag and amplifying overall performance. It is revealed that fluctuations in weight and center of gravity exert a substantial impact on the craft's resistance. The study adopts an integrated approach, incorporating Design of Experiment (DOE), Response Surface Method (RSM), and Computational Fluid Dynamics (CFD). Systematic adjustments to weight and center of gravity induce discernible effects on sinkage and hull trim, yielding distinctive resistance values. Empirical findings highlight that a marginal backward shift in the center of gravity, constituting approximately 1% of the vessel's length, culminates in a nearly 5% reduction in drag. However, immoderate backward or forward shifts precipitate an undesirable increase in resistance. This research underscores the versatility of the combined methodology in optimizing the center of gravity across diverse hulls or scenarios, with broader implications for enhancing the performance of high-speed planing crafts across varied contexts.

Keywords: Optimization method; Planing hull resistance; Weight configuration; Design of Experiment (DOE); Response Surface Method (RSM); Computational Fluid Dynamics (CFD)

1. Introduction

Global emissions reduction in the maritime sector should be taken seriously by implementing concrete efforts. According to the International Maritime Organization (IMO), the shipping sector is one of the largest sources of greenhouse gas emissions in the world, contributing to around 1,056 million tons or 2.9% of total global emissions in 2018[1)]. Emissions from the shipping sector mainly come from the burning of fossil fuels such as marine gas oil, diesel fuel, and residual fuel oil, which produce carbon dioxide (CO2), nitrogen oxide (NOx), sulfur dioxide (SO2), and fine particulate matter (PM)2). The primary contributor to global warming arises from the carbon emissions generated by fossil fuels, such as crude oil3,4). Fossil fuels are extensively utilized across various industrial sectors5,6) and transportation activities7). These fuels are combusted to produce thermal energy and pressure, subsequently employed to drive engines, generators, or steam turbines on ships8). To reduce emissions from the shipping sector, the IMO has implemented several regulations. One of these is the adoption of MARPOL regulations (International Convention for the Prevention of Pollution from Ships), which set limits on emissions from international ships9). Additionally, the IMO has introduced the IMO Strategy 2050, aiming to achieve a reduction of at least 50% in carbon dioxide emissions from the shipping sector by 2050 compared to the levels recorded in 200810).

The CO_2 emission from ships can be reduced in several ways7,11,12). First, through the use of alternative fuels such as liquefied natural gas (LNG)13,14), which emit 10% less than diesel oil15), or through other alternatives such as hydrogen16) and ammonia17,18). Second, by adopting zero-emission energy sources such as electric vessels19–21), solar-powered ships22,23), the use of sails24), and the use of kites25). Third, by implementing more efficient shipping practices such as reducing ship speed 26–28) and optimizing shipping routes26,29). Fourth, through the management of essential maintenance for the hydrodynamic performance of the ship, such as hull cleaning 30–36), propeller cleaning 37), and the use of more advanced antifouling methods 38–41). Fifth, through the use of tools to improve ship performance, such as ducted propellers42–44), boss cup fins45–48), stern flaps49–52), air bubble hull lubrication53), the use of super-smooth coatings54–56), and other Energy Saving Devices (ESD). Finally, at the hull designing stage, hull selection or modification can also be done so that drag are as minimal as possible57–62).

High-speed vessels or fast boats are recognized as among the most energy-intensive users due to their high energy consumption relative to the weight of the cargo they carry. These vessels are engineered for swift movement, resembling airplanes that aim to quickly transport cargo to their destinations. Analogously, high-speed vessels can be likened to sports cars, where the engine size is comparatively large compared to other components63). This design rationale is logical because the resistance faced by a boat is directly proportional to the square of its speed (V^2), while power is proportional to the cube of its speed (V^3)64). Hence, it is indisputable that high speeds entail the risk of heightened energy consumption, and even a minor reduction in resistance can prove advantageous in addressing emissions.

Fast boats are typically compact, rendering them highly responsive to alterations in weight65,66). These changes can easily result in shifts in their position and attitude, directly influencing their performance. To attain high speeds with minimal energy consumption, it is essential to meticulously design and fabricate the boat's heavy components, employing lightweight structural materials and powerful engines. Consequently, fluctuations in weight, encompassing both the quantity and the location of the center of weight, can profoundly influence the boat's position and attitude. These positional adjustments are identified as heave, while attitude adjustments are identified as pitch and roll. Heave pertains to the vertical translational motion of the boat (refer to Fig. 1a), pitch signifies the rotational motion around the transverse axis of the boat (refer to Fig. 1b), and roll indicates the rotational motion around the longitudinal axis of the boat. These alterations in the boat's orientation can impact resistance, performance, and overall stability.

Variations in trim and heave unequivocally yield performance alterations or resistances. Alterations in heave position stem from modifications in the ship's weight, while trim arises from shifts in the ship's center of gravity. Tran et al.67) conducted an optimization analysis on the design of a planing hull, incorporating diverse parameter variations such as ship weight (Δ) and Longitudinal Center of Gravity (l_{CG}). They achieved a noteworthy reduction in resistance, reaching up to -19.4%. Contrary to expectations, empirical findings from Fridsma's experiments revealed that a smaller l_{CG} (toward the aft) did not consistently lead to lower resistance68). Consequently, delving into the impacts of center of gravity position changes on planing resistance emerges as a compelling area of investigation.

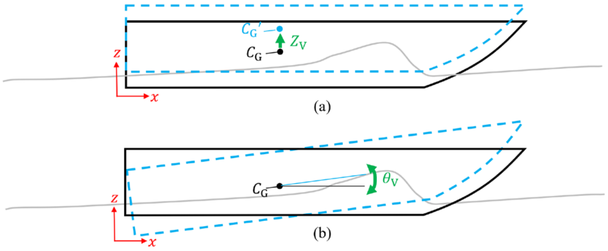

Fig. 1: The motions of planing vessels: (a) heave or sinkage, (b) pitch or trim.

Modifying the position and attitude of a planing vessel and employing a trim control device can significantly enhance its performance. The trim control can be in the form of a trim tab, interceptor, or stern foil, where the differences between the three are explained in Fig. 2. The trim control works by getting a lift force on the stern (transom) thereby causing a return moment as explained in Fig. 3. Avci and Barlas69) reported that interceptors demonstrate a drag reduction of 10 to 18% at speeds within the range of 0.5 < Fr < 0.85 and approximately 6% at speeds of 0.85 < Fr < 1. Nevertheless, beyond these speeds, interceptors prove ineffective and may even contribute to increased drag50). Additional studies exploring the utilization of interceptors can be found in the literature49,50,52,70,71). Similarly, trim tabs72–74) and stern foils51,75) have been identified as contributors to enhanced planing vessel performance within specified parameters.

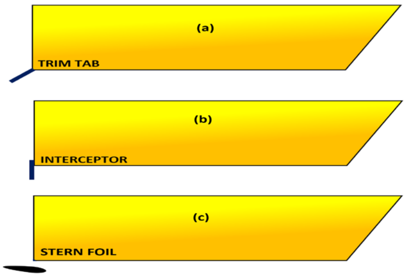

Fig. 2: Illustration of the differences in trim control: (a) trim tab, (b) interceptor, and (c) stern foil.

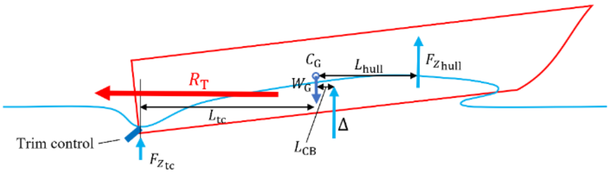

Fig. 3: Implementing trim control in planing boats.

The primary aim of this study is to optimize the performance of planing hulls by manipulating dynamic hull motions through adjustments in boat weight and center of gravity configuration, eliminating the necessity for additional tools like trim controls. Traditionally, the incorporation of a trim control device introduces extra weight, necessitating consideration and augmenting the overall weight of the boat due to the inclusion of mechanical components. Furthermore, the trim control device contributes to increased resistance as it submerges in water, thereby enlarging the wetted area. Hence, the author explores the feasibility of harnessing a naturally occurring trim control stemming from the boat's intrinsic weight, where the location of the center of gravity of the hull greatly impacts the planing ship's performance[76].

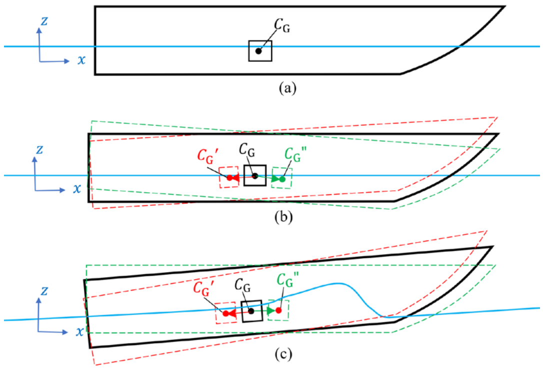

Fig. 4: Illustration of static changes in the center of gravity: (a) when the boat is not moving, (b) the center of gravity is changed when the boat is not moving, and (c) then the boat moves with the altered center of gravity from the beginning.

Generally, when the boat is at rest (not moving), the design ensures that the front and rear drafts are the same, which is called even keel (not trim), as depicted in Fig. 4a. However, manipulating the boat's center of gravity results in static trim, as illustrated in Fig. 4b. The occurrence of trim in a stationary boat is atypical. In Fig. **4**c, the boat exhibits altered performance due to a trim change from the outset. It would be more advantageous to possess technology capable of dynamically shifting the load while the boat is in motion, as depicted in Fig. 5. Fig. **5**a showcases the boat in a stationary position, Fig. **5**b presents the boat in motion, and Fig. **5**c illustrates intentional load shifting, resulting in alterations in the boat's attitude and consequent impacts on performance.

This study seeks to optimize boat performance by identifying the optimal weight configuration and center of gravity, utilizing Design of Experiments (DOE), Response Surface Methodology (RSM), and optimization techniques. DOE and RSM are well-established methods for analyzing cases involving multiple parameters[33,77–81]. DOE has become increasingly important in naval engineering and ship design, as modern tools enable optimization of hull forms and engine selection, potentially reducing ship drag by 12% and fuel consumption by up to 30%[82]. DOE method was also applied to improve the design of ship bows and has successfully reduced drag by up to 52%[83]. Not only for improving design performance, but DOE and RSM can also be used to create empirical formulas, such as predicting propeller performance[77], predicting increased frictional resistance due to roughness[33], and predicting the buckling strength of stiffened panels in the construction of surrogate models[84].

In this research, DOE and RSM methods are employed to formulate equations that assess the impact of trim and sinkage values on boat drag. Subsequently, the optimization method is applied to determine the trim and sinkage values associated with the minimum drag. The data utilized in this study are derived from Computational Fluid Dynamics (CFD) simulations, which have undergone rigorous verification and validation processes in accordance with guidelines from the International Towing Tank Conference (ITTC)[85].

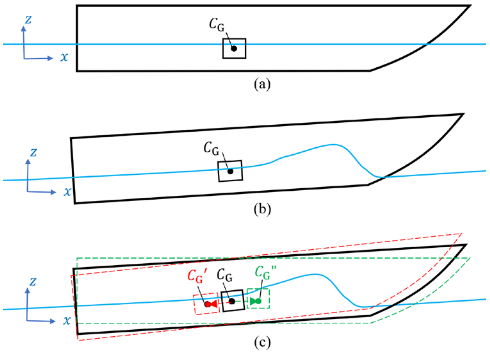

Fig. 5: Illustration of dynamic changes in the center of gravity: (a) when the boat is not moving, (b) when the ship is in motion, and (c) while the ship is moving, the center of gravity is dynamically altered.

2. Materials and methods

In the methodology of this study, the application of Design of Experiments (DOE), Response Surface Methodology (RSM), and optimization methods is elucidated in the diagram presented in Fig. 6. The overall steps of this work can be summarized as follows:

1) Ensuring the validity of CFD simulations by conducting verification and validation tests;
2) Utilizing the DOE method to vary the trim (Z_V) and sinkage (θ_V) parameters and collecting CFD data based on these variations;
3) Formulating an initial valid equation for the responses, which include total resistance (R_T), total lift force (F_Z), and moment ($L_{CG} \cdot F_Z$), which is then explained in Subsections 2.1 and 2.2;
4) Employing the RSM method to create parameter variations and collecting data (CFD simulations) to form nonlinear equations for each parameter;
5) Combining the initial equations from the step 3 with the parameter equations from the step 4, and validating the equations model against the previously obtained CFD data;
6) Varying the weight change configuration ($A\%$) and shift in center of gravity ($B\%$);
7) Predicting the new trim (Z_{V_i}) and sinkage (θ_{V_i}) resulting from the weight configuration variations;
8) Calculating the new total resistance (R_{T_i}) based on the new trim and sinkage;
9) Conducting the optimization process, where the objective function is to minimize drag ($\delta_{(R_T/\Delta)}\%$) through iterative changes in trim and sinkage, while satisfying the equilibrium conditions of forces ($\Sigma F_{\mathrm{Z}} = 0$) and moments ($\Sigma M_{\mathrm{Y}} = 0$). The optimization algorithm used is the Generalized Reduced Gradient (GRG) non-linear method by Lasdon et al.[86)], which is available in Microsoft Excel software.

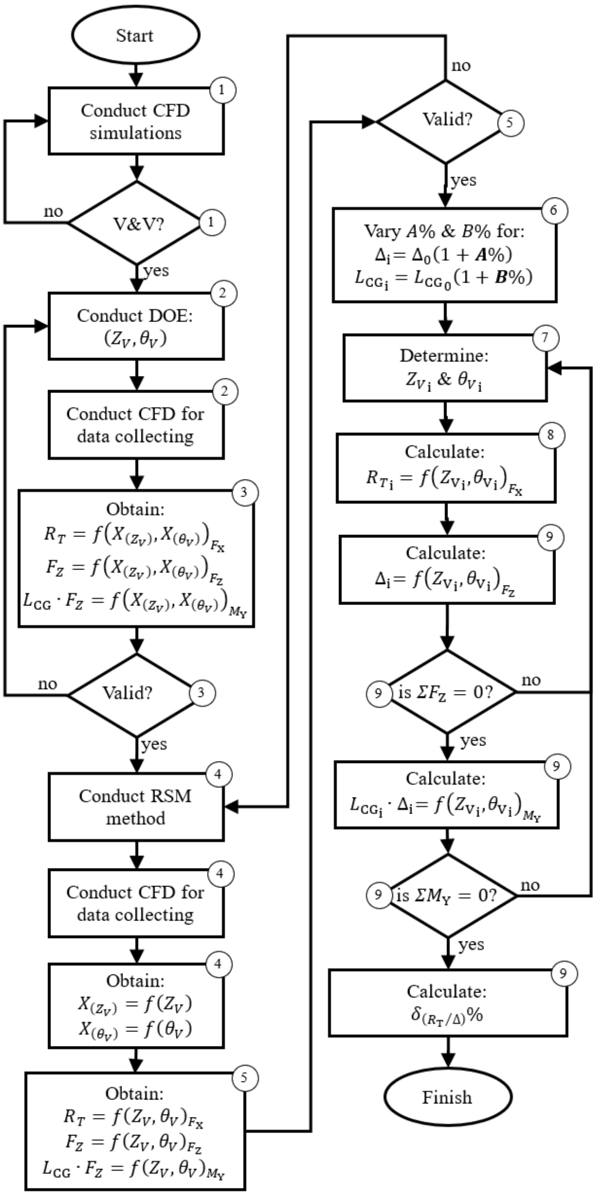

Fig. 6: Flowchart of the methods conducted in this research.

2.1.Forces equilibrium of planing hull

In simpler terms, Fig. **7** shows how various forces interact on the planing hull to create a balance of forces and moments. Along the boat's length (X axis), the thrust (T) produced by the thruster matches the total resistance (R_T), as explained in Equations (1) and (2). The total resistance (R_T) consists of the total resistance of water and air, each of which consists of pressure and friction force components. On the vertical axis of the boat (Z axis), the weight of the boat which is measured based on the displacement force value in Newton (Δ) is counteracted by the static (F_{st}) and dynamic (F_{dy}) forces. The static is very dominated by hydrostatic forces (buoyancy), while the dynamic consists of hydrodynamic and aerodynamic forces. Then, the force components acting in the Z-axis direction are explained in Equations (3) and (4). In the boat's transverse direction (Y axis), equilibrium moments arise from the static ($l_{st} \cdot F_{st}$) and dynamic ($l_{dy} \cdot F_{dy}$) moments acting against the moment of the boat weight ($l_{CG} \cdot \Delta$), as outlined in Equations (5) and (6).

$$\Sigma F_X = 0 \tag{1}$$

$$T - R_T = 0 \tag{2}$$

$$\Sigma F_Z = 0 \tag{3}$$

$$F_{st} + F_{dy} - \Delta = 0 \tag{4}$$

$$\Sigma M_Y = 0 \tag{5}$$

$$l_{st} \cdot F_{st} + l_{dy} \cdot F_{dy} + l_{CG} \cdot (-\Delta) = 0 \qquad (6)$$

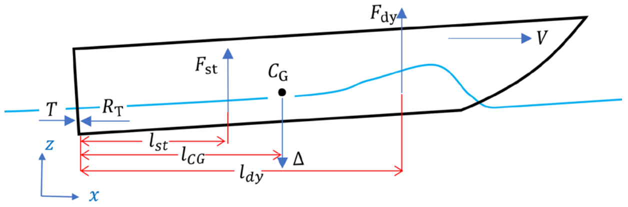

Fig. 7: A simple illustration depicting the forces acting on a planing hull.

2.2.Proposed model equations

The approach employed in this study aims to derive model equations for the boat's resistance based on trim and sinkage, while maintaining force and moment equilibrium. Utilizing the Design of Experiments (DOE) method, it is imperative to establish variations in trim, sinkage, and their combinations, as depicted in Fig. 8. The sinkage value is normalized by the length of the ship (Z_V/L) during this process. This normalization results in the derivation of three equations, contingent on the values of trim (θ_V) and sinkage (Z_V/L). The first equation represents the total resistance (R_T) (refer to Equation (7)), the second equation corresponds to the total lift force or equivalent weight of the boat (Δ) (refer to Equations (8) and (9)), and the final equation describes the equivalent lift moment, equating to the weight moment ($l_{CG} \cdot \Delta$) (refer to Equations (10) and (11)). Subsequently, values for R_T, F_{st}, F_{dy}, l_{st}, and l_{dy} will be obtained through Computational Fluid Dynamics (CFD) simulation as required data for formulating the model equations.

$$R_T = f\left(\frac{Z_V}{L}, \theta_V\right)_{F_X} \qquad (7)$$

$$F_{st} + F_{dy} = f\left(\frac{Z_V}{L}, \theta_V\right)_{F_Z} \qquad (8)$$

$$\Delta = f\left(\frac{Z_V}{L}, \theta_V\right)_{F_Z} \qquad (9)$$

$$l_{st} \cdot F_{st} + l_{dy} \cdot F_{dy} = f\left(\frac{Z_V}{L}, \theta_V\right)_{M_Y} \qquad (10)$$

$$l_{CG} \cdot \Delta = f\left(\frac{Z_V}{L}, \theta_V\right)_{M_Y} \qquad (11)$$

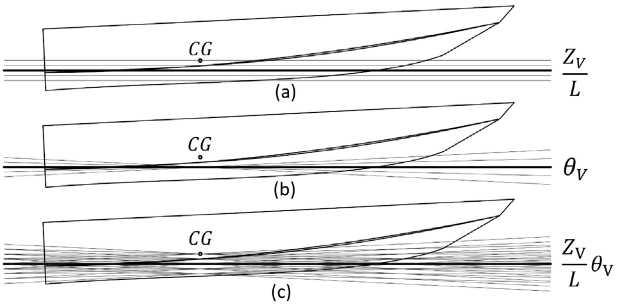

Fig. 8: Differences in (a) sinkage, (b) trim, and (c) both combinations result in varying draft positions.

2.3.Objective function

The objective function in this context is the equation necessary for determining the optimal value of parameter iterations that adheres to the specified boundary conditions[87]. The formulated objective function is articulated in Equations (12) and (13). In Equation (12), $\delta(R_T/\Delta_0)\%$ denotes the alteration in resistance resulting from the adjusted sinkage and trim parameters relative to the initial design conditions. Equation (13) expresses $\delta(R_T/\Delta_i)\%$, representing the variation in performance (resistance-to-weight ratio) compared to the original hull performance.

The value R_{T_i} is the total resistance of the ship with the functions of sinkage and trim as formulated in Equation (14). Whereas, Z_{V_i} and θ_{V_i} represent the changed values of sinkage and trim resulting from the iterations of the optimization process. The value of R_{T_0} corresponds to the resistance at the initial design condition based on the initial sinkage and trim as formulated in Equation (15).

$$\delta(R_T/\Delta_0)\% = \left\{\left(\frac{R_{T_i} - R_{T_0}}{R_{T_0}}\right)/\Delta_0\right\} \times 100\% \qquad (12)$$

$$\delta(R_T/\Delta_i)\% = \frac{(R_{T_i}/\Delta_i) - (R_{T_0}/\Delta_0)}{(R_{T_0}/\Delta_0)} \times 100\% \qquad (13)$$

$$R_{T_i} = f\left[\left(\frac{Z_{V_i}}{L}\right), \left(\theta_{V_i}\right)\right]_{|(F_X)} \qquad (14)$$

$$R_{T_0} = f\left[\left(\frac{Z_{V_0}}{L}\right), \left(\theta_{V_0}\right)\right]_{|(F_X)} \qquad (15)$$

Next, the values of Z_{V_i} and θ_{V_i} must result in a lift value equivalent to the new displacement (Δ_i), as formulated in Equation (16). The lift and displacement values should be equal to ensure force balance along the Z-axis, $\sum F_Z = 0$. The new displacement value can be calculated using Equation (17), where $A\%$ represents the change in weight value. The value of $A\%$ represents the variation in the weight of the ship determined in this study, where the weight of the ship is varied from -10% to +10%.

$$f^{-1}\left[\left(\frac{Z_{V_i}}{L}\right),\left(\theta_{V_i}\right)\right]_{|(F_Z)} = \Delta_i \tag{16}$$

$$\Delta_i = \Delta_0(1 + A\%) \tag{17}$$

The changes in the new sinkage and trim conditions certainly lead to adjusted moment values in accordance with the moment values of $L_{CG_i} \cdot \Delta_i$. The value of L_{CG_i} represents the new center of gravity position resulting from variations in the center of gravity shift represented by $B\%$, as shown in Equation (19). The hydrodynamic moments generated by the new sinkage and trim must be equal to the weight moments with the new center of gravity position to ensure moment balance along the y-axis, $\sum M_Y = 0$. Therefore, all the new values of sinkage and trim, in order to find the resistance value, must satisfy the force balance along the Z-axis and moment balance along the Y-axis, as formulated in Equation (20).

$$f^{-1}\left[\left(\frac{Z_{V_i}}{L}\right),\left(\theta_{V_i}\right)\right]_{|(M_Y)} = L_{CG_i} \cdot \Delta_i \tag{18}$$

$$L_{CG_i} = L_{CG_0}(1 + B\%) \tag{19}$$

$$\begin{aligned}\left[\left(\frac{Z_{V_i}}{L}\right),\left(\theta_{V_i}\right)\right]_{|(F_X)} &= \left[\left(\frac{Z_{V_i}}{L}\right),\left(\theta_{V_i}\right)\right]_{|(F_Z)} \\ &= \left[\left(\frac{Z_{V_i}}{L}\right),\left(\theta_{V_i}\right)\right]_{|(M_Y)}\end{aligned} \tag{20}$$

Table 1 The C-hull model parameters from Taunton et al.[88] serve as an object of study in this research.

Parameter	**Symbol**	**Value**	**Unit**
Length overall	L	2.00	m
Beam	B	0.46	m
Draught	T	0.09	m
Volume Displacement	∇	0.027	m^3
Displaced weight Force	Δ	243.40	N
Length/cube root of the displaced volume	$L/\nabla^{1/3}$	6.86	
Length overall/beam	L/B	4.35	
Deadrise angle	β	22.50	degree
Longitudinal center of gravity	l_{CG}	33.00	%L

2.4.Hull model data

The hull model used in this study is the C hull model from Taunton et al. [88]. The planing craft model with these parameters will be the reference value to improve its performance with variations in weight and center of gravity configurations. The properties of the hull are described in Table 1. The geometric model of this hull can be downloaded on the reference page, so that repeated or further testing and research can be carried out[88].

2.5.CFD simulation

2.5.1. Computational settings

In this study, CFD simulations using the governing equations based on an unsteady Reynolds-Averaged Navier-Stokes (uRANS) were employed to acquire the necessary data. The conservation of mass and momentum equations are solved with a commercial CFD software, ANSYS FLUENT. The average continuity and momentum equations are given in Equations (21) and (22). Where: U_i is the average speed component; $\bar{P}$ is the average pressure; ρ is the effective density of the fluid; μ is the effective viscosity; u_i' is the fluctuation velocity component; $\rho\overline{U_i'U_j'}$ is the Reynolds stress, $\overline{\tau_{ij}}$ is the tensor component of the mean viscous stress[89], as given in Equation (23).

$$\frac{\partial(\rho\overline{U_i})}{\partial x_i} = 0 \tag{21}$$

$$\frac{\partial(\rho\overline{U_i})}{\partial t} + \frac{\partial}{\partial x_i}\left(\rho\overline{U_i}\,\overline{U_j} + \rho\overline{U_i'U_j'}\right) = -\frac{\partial\bar{P}}{\partial x_i} + \frac{\partial\overline{\tau_{ij}}}{\partial x_j} \tag{22}$$

$$\overline{\tau_{ij}} = \mu\left(\frac{\partial\overline{U_i}}{\partial x_j} + \frac{\partial\overline{U_j}}{\partial x_i}\right) \tag{23}$$

$$\alpha(\vec{x},t) = \begin{cases}\Delta_1, \vec{x}, \in V_1 \\ \Delta_0, \vec{x}, \in V_2\end{cases} \tag{24}$$

In this simulation, the VOF (volume of fluid) method was utilized to capture the influence of a free surface on the computational model. The VOF technique was well-suited for representing multiple distinct flow phases. The water and air fluid domains were characterized by the volume fraction attribute in Equation (24), where V denotes the designated computational domain, V_1 represents the volume of fluid 1, and V_2 represents the volume of fluid 2. Each grid cell was assigned a volume fraction value of either 1 or 0 to distinguish between the air and water fluids[90].

The turbulence model selected for this study was the SST (Shear Stress Transport) k-ω model. This model incorporates the k-ω wall function, which is specifically designed for accurate modeling near the wall region. It captures the turbulent flow characteristics in this region effectively. Additionally, the model also includes the k-ε model, which is suitable for modeling the far field of the flow domain. By combining these two models, the SST k-ω model provides a comprehensive representation of turbulence throughout the entire flow field[91].

Accurate selection of the time step value is crucial when conducting simulations that exhibit instability, as it directly influences the Courant number. To ensure reliable results, the ITTC (International Towing Tank Conference) provides a recommended time step range of $\Delta t = 0.005 - 0.01L/V$[92], where L represents the length of hull, and V represents the boat velocity. Adhering to this guideline, the present simulation is performed with a time step value within the recommended range, guaranteeing the reliability of the obtained results. Proper consideration of the time step helps maintain numerical stability and captures transient phenomena accurately during the simulation.

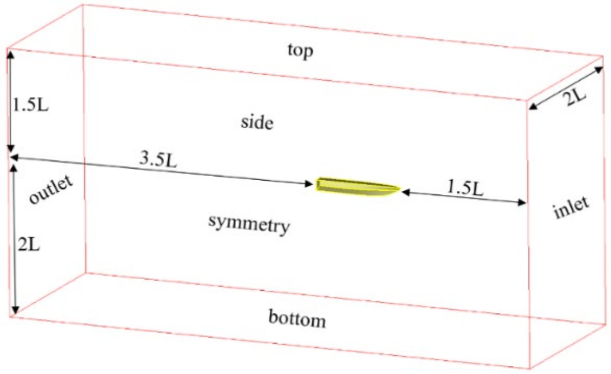

Fig. 9: Setting the size of the domain and the boundary conditions employed.

2.5.2. Domain and boundary condition settings

The boundary conditions and size of the computational domain were determined according to the illustration shown in Fig. 9. For the inlet, a velocity inlet boundary condition was applied to accommodate multiple fluids entering the domain. On the other hand, the outlet was set as a pressure outlet boundary condition for the multiple fluids exiting the domain. The hull model was created as a half-model and then split with a symmetry plane, which was defined as a symmetry boundary to exploit the symmetry of the problem. The hull model was assigned a no-slip condition, ensuring that the fluid velocity is zero at the solid surface. The top, bottom, and sides of the domain were set to a free-slip condition, allowing tangential flow but preventing normal flow through these boundaries[93)]. To account for the body motion of the hull model, a fixed or static mesh approach was adopted. The efficacy of the fixed mesh method was evaluated by Doustdar and Kazemi[94)], and the results were found to be comparable to those obtained using the dynamic mesh method, suggesting that the fixed mesh approach is sufficient for this simulation.

2.5.3. Mesh generation

To assess the uncertainty of numerical simulations, a grid independence test is conducted [95)], which involves utilizing three different mesh sizes: coarse, medium, and fine. In this test, each mesh is refined by dividing it in half. Consequently, a medium mesh contains twice as many elements as a coarse mesh. Similarly, a fine mesh has twice the number of elements as a medium mesh. This progressive refinement allows for evaluating the sensitivity of the simulation results to the mesh size and determining the point at which further mesh refinement does not significantly impact the results.

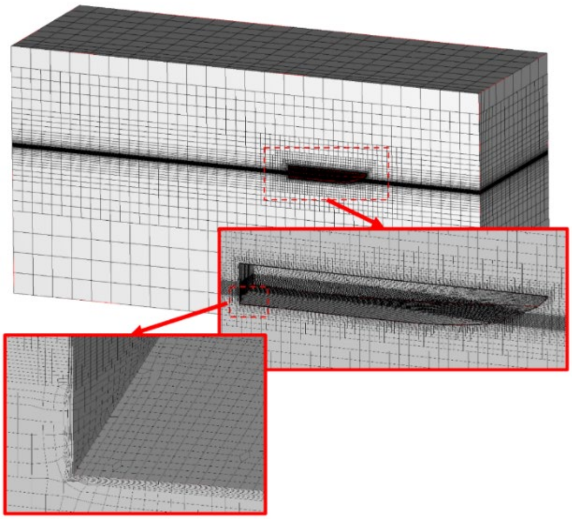

Fig. 10: Mesh and inflation layer generation for the medium configuration (2.5 million).

The arrangement of the mesh must comply with the guidelines for modeling turbulent flow using the selected turbulence model. In order to accurately apply the wall function approach (where, $30 < y^+ < 300$), the initial mesh distance was set to approximately 60 units of y^+. Additionally, the mesh was configured to include an inflation layer. A visual representation of the mesh arrangement can be seen in Fig. 10, providing an overview of the mesh structure and its characteristics. This information is crucial for understanding the specifics of the mesh design and its adherence to the requirements of the turbulent flow simulation.

2.6.Design of experiment (DOE) method calculation

In this study, the type of Design of Experiments (DOE) employed is the Two-level Full Factorial Design. With only two parameters involved, a total of 2^2 or 4 specimens are required to collect the necessary data[96)]. Consequently, four different combinations of specimens will be simulated using CFD software. Each of these specimens will provide three crucial response variables: drag, lift, and moment. Hence, at this stage, there is a total of 4 × 3 or 12 data points that need to be processed. The DOE methodology enables a systematic and efficient approach to collect and analyze the required data while minimizing the number of experiments conducted.

The values for the parameters, assigned as the upper (high) and lower (low) levels, are described in

Table 2. The lower values are determined based on the ship's position and attitude when even keel, while the upper values are determined when the hull is in the initial design position and attitude resulting from experiments conducted by Taunton et al.[88)] at that speed. Determining these two boundaries is crucial as it will affect the interpolated parameter values and may even lead to extrapolation.

The response equations that will be formulated later are represented by Equation (25), where Y denotes the responses, $\beta_{(0)}$ denotes the grand average derived from the initial data, $\beta_{(\mathrm{i})}$ signifies the effect value of each parameter, and $\mathrm{X}_{(\mathrm{i})}$ represents the weight of the parameter. The $\beta_{(\mathrm{i})}$ value is obtained by taking the average product when $Y_{(\mathrm{i})}$ is multiplied by $X_{(\mathrm{i})}$. For a more comprehensive explanation, please refer to the literatures[33,78].

$$Y = \beta_{(0)} + \beta_{\left(\frac{z_V}{L}\right)} \cdot X_{\left(\frac{z_V}{L}\right)} + \beta_{(\theta_V)} \cdot X_{(\theta_V)} + \beta_{\left(\frac{z_V}{L}\theta_V\right)} \cdot X_{\left(\frac{z_V}{L}\theta_V\right)} \tag{25}$$

2.7.Response surface method (RSM) calculation

In order to determine the functional form of each weighted parameter ($X_{(\mathrm{i})}$), the Response Surface Method (RSM) was employed. To account for potential non-linearity in the function, additional values for each parameter were determined and presented in Table 3. These additional values, namely Midpoint, High+, and High++, were introduced to facilitate extrapolation of the equation and capture a wider range of response results[33]. The determination of adding points is actually flexible, whether it is interpolation (between -1 and +1) or extrapolation. Then, CFD simulations need to be conducted for each of these new parameter combinations to acquire the required data. Polynomial regression analysis will then be utilized to examine the relationship between the obtained data and the formulated equations. By adopting this approach, a comprehensive evaluation of the response outcomes and their correlation with the specified equations can be achieved, taking into consideration the potential non-linear behavior of the system.

Table 2 Analyzing the variation in the values of the parameters.

	Parameters	Symbol, (i)	Initial condition	Low, $X_{(\mathrm{i})} = -1$	High, $X_{(\mathrm{i})} = +1$
a	Dynamic sinkage at CG/ Length overall	Z_{V}/L	$\frac{0.04}{2} = 0.02$	$\frac{0.00}{2} = 0.00$	$\frac{0.04}{2} = 0.02$
b	Dynamic trim angle [°]	θ_{V}	2.67	0.00	2.67

Table 3 Determination of the midpoint and extrapolated value for each parameter in the RSM method.

	Parameters	Symbol, (i)	Low, $X_{(\mathrm{i})} = -1$	Midpoints, $-1 < X_{(\mathrm{i})} < +1$	High, $X_{(\mathrm{i})} = +1$	High^{+}, $X_{(\mathrm{i})} > +1$	High^{++}, $X_{(\mathrm{i})} > +1$
a	Dynamic sinkage at CG/ Length overall	Z_V/L	0.00	0.01	0.02	0.03	0.04
b	Dynamic trim angle [°]	θ_V	0.00	1.335	2.67	4.005	5.34

3. Results and discussions

3.1.CFD simulation results

This subsection focuses on the outcomes of the CFD simulation work, encompassing the verification test, validation test, and analysis of the results. The specific results obtained from the simulations include drag (F_X), lift (F_Z), and moment (M_Y). These parameters provide crucial insights into the forces and moments experienced by the system under investigation. The verification test ensures that the simulation setup is correctly implemented and produces reliable results, while the validation test assesses the accuracy of the simulation by comparing it to experimental or theoretical data. The analysis of the results aids in understanding the behavior of the system and drawing meaningful conclusions from the simulation work.

3.1.1. CFD verification study

To evaluate the potential inaccuracies in both space and time of the simulations, convergence studies were conducted. In order to estimate the numerical uncertainties, the Grid Convergence Index (GCI) method based on Generalized Richardson Extrapolation [97]. The GCI method involves calculating the ratio of the error between two different grid resolutions, which provides valuable information about the rate at which the error decreases as the resolution increases. According to Celik et al.[98], the sequence of calculation for this method is as follows:

$$p_a = \frac{1}{\ln(r_{21})}\left|\ln\left|\frac{\varepsilon_{32}}{\varepsilon_{21}}\right| + q(p_a)\right| \tag{26}$$

$$q(p_a) = \ln\left(\frac{r_{21}^{p_a} - s}{r_{32}^{p_a} - s}\right) \tag{27}$$

$$s = \mathrm{sign}\left(\frac{\varepsilon_{32}}{\varepsilon_{21}}\right) \tag{28}$$

Where, r_{21} and r_{32} are refinement factors given by $r_{21} = \sqrt[3]{N_1/N_2}$ for a spatial convergence study of a 3D model. convergence study. N_i are the cell number. $\varepsilon_{32} = \emptyset_3 - \emptyset_2$, $\varepsilon_{21} = \emptyset_2 - \emptyset_1$, and $\emptyset_i$ denotes the simulation result, i.e., R_{T}/Δ in this study.

The extrapolated value is calculated by:

$$\emptyset_{ext}^{21} = \frac{r_{21}^{p}\emptyset_1 - \emptyset_2}{r_{21}^{p} - 1} \tag{29}$$

The approximate relative error, e_a^{21}, is obtained by:

$$e_a^{21} = \left|\frac{\emptyset_1-\emptyset_2}{\emptyset_1}\right| \tag{30}$$

The extrapolated relative error, e_{ext}^{21}, is obtained by:

$$e_{ext}^{21} = \left|\frac{\emptyset_{ext}^{21}-\emptyset_1}{\emptyset_{ext}^{21}}\right| \tag{31}$$

Finally, the fine-grid convergence index is found by:

$$GCI_{fine}^{21} = \frac{1.25e_a^{21}}{r_{21}^{p}-1} \tag{32}$$

The result of numerical uncertainty calculation was obtained as 1.73%, with the detailed calculation shown in Table 4.

Table 4 Parameters employed for calculating the discretization error in the spatial convergence study.

Parameter	**Value**	**Parameter**	**Value**
N_1 (Coarse)	1.2×10⁶	ε_{32}	-0.0004
N_2 (Medium)	2.5×10⁶	ε_{21}	-0.0007
N_3 (Fine)	5.5×10⁶	s	1.0000
r_{21}	1.2700	e_a^{21}	0.0037
r_{32}	1.3054	q	-0.1231
$\emptyset_1$	0.1874	p_a	2.8563
$\emptyset_2$	0.1867	$\emptyset_{ext}^{21}$	0.1900
$\emptyset_3$	0.1863	e_{ext}^{21}	1.36%
		GCI_{fine}^{21}	1.73%

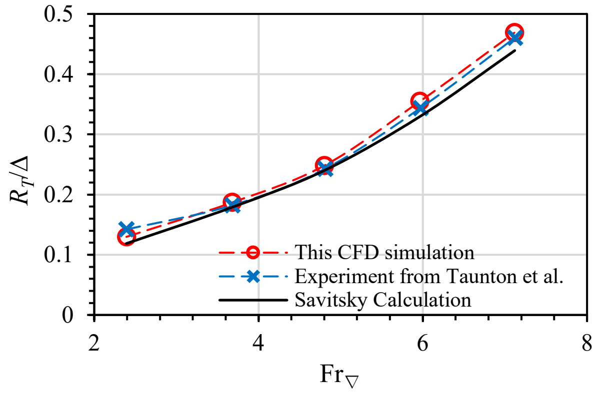

Fig. 11: Validation test results comparing with Taunton et al. [88] and Savitsky[99].

3.1.2. CFD validation study

This CFD simulation was validated with experimental tests. The experimental results being compared are the results of research from Taunton et al.[88] using the precise same hull model, namely the hull C model. The calculations using the empirical method from Savitsky[99] were also provided. All three of them are presented in the graph in Fig. 11. The errors are calculated using Equation (33) to assess the precision of current CFD results. Experimental and numerical data are indicated by the subscripts EXP and CFD, respectively. Equation (34) calculates RMSE (Root Mean Square Error), which measures the errors of the samples based on the speed variations. Therefore, the error result of this simulation modeling on the experimental results is 4.45%, as shown in Table 5.

$$E_{(R_T/\Delta)}\% = \frac{(R_T/\Delta)_{CFD}-(R_T/\Delta)_{EXP}}{(R_T/\Delta)_{EXP}} \times 100\% \tag{33}$$

$$\mathrm{RSME} = \sqrt{\sum_{i=1}^{N}\frac{(E^2)}{N}} \tag{34}$$

Table 5 Summary of the errors observed in different CFD models employed in the current research.

Fr_∇	**$(R_T/\Delta)_{EXP}$**	**$(R_T/\Delta)_{CFD}$**	**$E_{(R_T/\Delta)}\%$**
2.39	0.1419	0.1297	-8.58
3.68	0.1821	0.1867	2.56
4.80	0.2427	0.2480	2.18
5.96	0.3435	0.3546	3.25
7.12	0.4604	0.4688	1.83
RSME			4.45

In this analysis, the uncertainty value (U_V) was determined using the methodology outlined by ITTC (2008). The calculation of U_V was performed using the equation provided below:

$$U_V^2 = U_D^2 + U_{SN}^2 \tag{35}$$

Where U_D represents the uncertainty of the experimental results, and U_{SN} represents the numerical uncertainty. Based on Taunton et al. (2010), the experimental uncertainty is ~3.2%. According to the section of Verification study, the value of U_{SN} is 1.73%. Thus, using Equation (35), the uncertainty value for this analysis was U_V = 3.64%.

3.2.Design of experiment (DOE) method results

All specimens, along with the CFD simulation results and the corresponding effect ($\beta_{(i)}$)calculations, which were varied based on the DOE method, are tabulated in Table 6. The CFD simulation results, also known as responses, are presented in a non-dimensional form. Therefore, the drag is represented as R_T/Δ, where the drag force divided by displacement. The lift is represented as F_Z/Δ, where the lift force divided by displacement. The moment is represented as $M_Y/(\Delta \cdot L)$, where the moment divided by the product of displacement and boat's length. The calculated effect $\beta_{(i)}$ values of each parameter for each response are also presented.

The effect $\beta_{(i)}{}_{|R_T/\Delta|}$ value represents the effect of parameters on the response of drag. In the case of the drag response (R_{T}/Δ), the sinkage (Z_{V}) has a negative effect (-0.0867), indicating that increasing the sinkage value will decrease the drag. Similarly, the trim (θ_{V}) has a negative effect (-0.0007), meaning that an increase in trim will result in a decrease in drag. The significance of the sinkage effect is more pronounced than the trim effect, indicating that making changes to the sinkage will have a greater influence on drag compared to adjusting the trim.

On the other hand, different trends are observed in the effect $\beta_{(\mathrm{i})|F_Z/\Delta|}$ values for the lift response. In the lift response (F_{Z}/Δ), the effect of trim is positive (0.2581), indicating that increasing the trim value will lead to an increase in lift. In contrast, the effect of sinkage on the lift response is negative (-0.3316), indicating that an increase in sinkage will lead to a decrease in lift force. It is evident that the trim effect is more prominent than the sinkage effect, suggesting that adjusting the trim value has a greater impact on increasing lift compared to modifying the sinkage value.

Regarding the moment response ($M_{\mathrm{Y}}/(\Delta \cdot L)$), both parameters have positive effects, with the sinkage parameter being more dominant. Therefore, changing the sinkage value is the most effective approach to modify the moment value.

The response equations for R_T/Δ are explained in Equations (36) and (37). The response equations for F_{Z}/Δ are explained in Equations (38) and (39). The response equations for $M_{\mathrm{Y}}/(\Delta \cdot L)$ are explained in Equations(40) and (41).

The equation form of the model for the drag response is given by:

$$R_{\mathrm{T}}/\Delta = \beta_{(0)\left|\frac{R_{\mathrm{T}}}{\Delta}\right|} + \beta_{\left(\frac{Z_{\mathrm{V}}}{L}\right)\left|\frac{R_{\mathrm{T}}}{\Delta}\right|} \cdot X_{\left(\frac{Z_{\mathrm{V}}}{L}\right)} + \beta_{(\theta_{\mathrm{V}})\left|\frac{R_{\mathrm{T}}}{\Delta}\right|} \cdot X_{(\theta_{\mathrm{V}})} + \beta_{\left(\frac{Z_{\mathrm{V}}}{L}\theta_{\mathrm{V}}\right)\left|\frac{R_{\mathrm{T}}}{\Delta}\right|} \cdot X_{\left(\frac{Z_{\mathrm{V}}}{L}\right)} \cdot X_{(\theta_{\mathrm{V}})} \tag{36}$$

The equation for predicting drag is derived by incorporating the obtained values of the effect coefficients as follows:

$$R_{\mathrm{T}}/\Delta = 0.2587 - 0.0867 \cdot X_{\left(\frac{Z_{\mathrm{V}}}{L}\right)} - 0.0007 \cdot X_{(\theta_{\mathrm{V}})} + 0.0155 \cdot X_{\left(\frac{Z_{\mathrm{V}}}{L}\right)} \cdot X_{(\theta_{\mathrm{V}})} \tag{37}$$

Secondly, the equation for the lift response is formulated using the following approach:

$$F_{\mathrm{Z}}/\Delta = \beta_{(0)\left|\frac{F_{\mathrm{Z}}}{\Delta}\right|} + \beta_{\left(\frac{Z_{\mathrm{V}}}{L}\right)\left|\frac{F_{\mathrm{Z}}}{\Delta}\right|} \cdot X_{\left(\frac{Z_{\mathrm{V}}}{L}\right)} + \beta_{(\theta_{\mathrm{V}})\left|\frac{F_{\mathrm{Z}}}{\Delta}\right|} \cdot X_{(\theta_{\mathrm{V}})} + \beta_{\left(\frac{Z_{\mathrm{V}}}{L}\theta_{\mathrm{V}}\right)\left|\frac{F_{\mathrm{Z}}}{\Delta}\right|} \cdot X_{\left(\frac{Z_{\mathrm{V}}}{L}\right)} \cdot X_{(\theta_{\mathrm{V}})} \tag{38}$$

As a result, the following equation can be utilized to predict the lift response:

$$F_{\mathrm{Z}}/\Delta = 0.9501 - 0.3316 \cdot X_{\left(\frac{Z_{\mathrm{V}}}{L}\right)} + 0.2581 \cdot X_{(\theta_{\mathrm{V}})} + 0.0064 \cdot X_{\left(\frac{Z_{\mathrm{V}}}{L}\right)} \cdot X_{(\theta_{\mathrm{V}})} \tag{39}$$

Thirdly, in the case of the moment response, the equation formulation is as follows:

$$\frac{M_{\mathrm{Y}}}{\Delta.L} \times 10^{-3} = \beta_{(0)\left|\frac{M_{\mathrm{Y}}}{\Delta.L}\right|} + \beta_{\left(\frac{Z_{\mathrm{V}}}{L}\right)\left|\frac{M_{\mathrm{Y}}}{\Delta.L}\right|} \cdot X_{\left(\frac{Z_{\mathrm{V}}}{L}\right)} + \beta_{(\theta_{\mathrm{V}})\left|\frac{M_{\mathrm{Y}}}{\Delta.L}\right|} \cdot X_{(\theta_{\mathrm{V}})} + \beta_{\left(\frac{Z_{\mathrm{V}}}{L}\theta_{\mathrm{V}}\right)\left|\frac{M_{\mathrm{Y}}}{\Delta.L}\right|} \cdot X_{\left(\frac{Z_{\mathrm{V}}}{L}\theta_{\mathrm{V}}\right)} \tag{40}$$

Then, the following is the outcome of formulating the equation to predict the moment response:

$$\frac{M_{\mathrm{Y}}}{\Delta.L} \times 10^{-3} = -38.89 + 38.18 \cdot X_{\left(\frac{Z_{\mathrm{V}}}{L}\right)} + 0.0413 \cdot X_{(\theta_{\mathrm{V}})} + 0.04 \cdot X_{\left(\frac{Z_{\mathrm{V}}}{L}\right)} \cdot X_{(\theta_{\mathrm{V}})} \tag{41}$$

Table 6 The Design of Experiments (DOE) matrix, comprising parameter combinations, and the retrieval of data results from CFD simulations for each response.

Model Label	**Comb**	$\boldsymbol{X_{(\mathrm{i})}}$			$\boldsymbol{R_{\mathrm{T}}/\Delta}$	$\boldsymbol{\beta_{(\mathrm{i})\left\|\frac{R_T}{\Delta}\right\|}}$	$\boldsymbol{F_{\mathrm{Z}}/\Delta}$	$\boldsymbol{\beta_{(\mathrm{i})\left\|\frac{F_Z}{\Delta}\right\|}}$	$\boldsymbol{M_{\mathrm{Y}}/\Delta.L}$ **(×10^{-3})**	$\boldsymbol{\beta_{(\mathrm{i})\left\|\frac{M_Y}{\Delta.L}\right\|}}$
		$\boldsymbol{X_{\left(\frac{Z_V}{L}\right)}}$	$\boldsymbol{X_{(\theta_V)}}$	$\boldsymbol{X_{\left(\frac{Z_V}{L}\right)}.X_{(\theta_V)}}$						
C_0	0	-1	-1	+1	0.3617	0.2587	1.03	0.9501	-76.25	-38.89
C_a	Z_{V}/L	+1	-1	-1	0.1572	-0.0867	0.354	-0.3316	-16.38	38.18
C_b	θ_{V}	-1	+1	-1	0.3292	-0.0007	1.5334	0.2581	-77.89	7.43
C_ab	$Z_{\mathrm{V}}/L\ \theta_{\mathrm{V}}$	+1	+1	+1	0.1867	0.0155	0.8831	0.0064	14.98	8.25

3.3.Response surface method (RSM) results

This chapter unveils the results of the function formulation for each parameter (Z_V/L and θ_V), corresponding to the three responses: R_T/Δ, F_Z/Δ, and $M_Y/(\Delta \cdot L)$. Tables 7 and 8 present the outcomes of the Response Surface Method (RSM) for the sinkage parameter and trim parameter, respectively. The weight of the $X_{(i)}$ parameter value is determined based on the proportionality observed in the Computational Fluid Dynamics (CFD) simulation results. The subsequent section illustrates the outcomes of formulating a function for each parameter (Z_V/L and θ_V) concerning the three responses—R_T/Δ, F_Z/Δ, and $M_Y/(\Delta \cdot L)$.

Table 7 and Table 8 show the results of the RSM for the sinkage parameter and trim parameter, respectively. The weight of parameter values $X_{(i)}$ was established based on the CFD simulation results. For example, in Table 7, the value $X_{(Z_V/L)|R_T/\Delta|}$ for Low and High are locked at values -1 and 1. Then, the Medium, High^{+} and High^{++} values are determined using a polynomial curve fitting to match the R_T/Δ response due to the Z_V/L or θ_V variables. The same treatment was also carried out for the lift and moment response. Therefore, the function results for each parameter for each response are described in Fig. 12 to Fig. 14 and Equations (42) to (47).

The results of non-linear regression from order 2 to order 4 are shown in Fig. 12 to Fig. 14. The equation of order 2 is referred to as y₁, the equation of order 3 is referred to as y₂, and the equation of order 4 is referred to as y₃. Each equation, with its respective order, will be tested for accuracy validation in the next subsection.

Table 7 The results of data obtained from CFD simulations for predicting the sinkage parameter equation.

Model Label	**Position**	Z_V/L	θ_V	R_T/Δ	$X_{\left(\frac{Z_V}{L}\right)\left\|\frac{R_T}{\Delta}\right\|}$	F_Z/Δ	$X_{\left(\frac{Z_V}{L}\right)\left\|\frac{F_Z}{\Delta}\right\|}$	$\frac{M_Y \times (10^{-3})}{\Delta.L}$	$X_{\left(\frac{Z_V}{L}\right)\left\|\frac{M_Y}{\Delta.L}\right\|}$
C_a(-1)	Low	0.00	2.67	0.3292	-1.00	1.5334	-1.00	-77.89	-1.00
C_a(0)	Medium	0.01		0.2493	0.13	1.1897	0.07	-39.97	-0.20
C_a(+1)	High	0.02		0.1867	1.00	0.8831	1.00	14.98	1.00
C_a(+2)	High+	0.03		0.1320	1.78	0.5955	1.90	63.35	2.03
C_a(+3)	High+ +	0.04		0.0669	2.73	0.2594	2.93	46.57	1.65

Table 8 The results of data obtained from CFD simulations for predicting the trim parameter equation.

Model Label	**Position**	Z_V/L	θ_V	R_T/Δ	$X_{(\theta_V)\left\|\frac{R_T}{\Delta}\right\|}$	F_Z/Δ	$X_{(\theta_V)\left\|\frac{F_Z}{\Delta}\right\|}$	$\frac{M_Y \times (10^{-3})}{\Delta.L}$	$X_{(\theta_V)\left\|\frac{M_Y}{\Delta.L}\right\|}$
C_b(-1)	Low	0.02	0.00	0.1572	-1.0	0.3540	-1.00	-16.3801	-1.00
C_b(0)	Medium		1.34	0.1692	-0.2	0.5748	-0.15	-3.1538	-0.15
C_b(+1)	High		2.67	0.1867	1.0	0.8831	1.00	14.9761	1.00
C_b(+2)	High+		4.01	0.2241	3.6	1.2289	2.35	35.9273	2.30
C_b(+3)	High+ +		5.34	0.2838	7.7	1.6075	3.75	59.3753	3.78

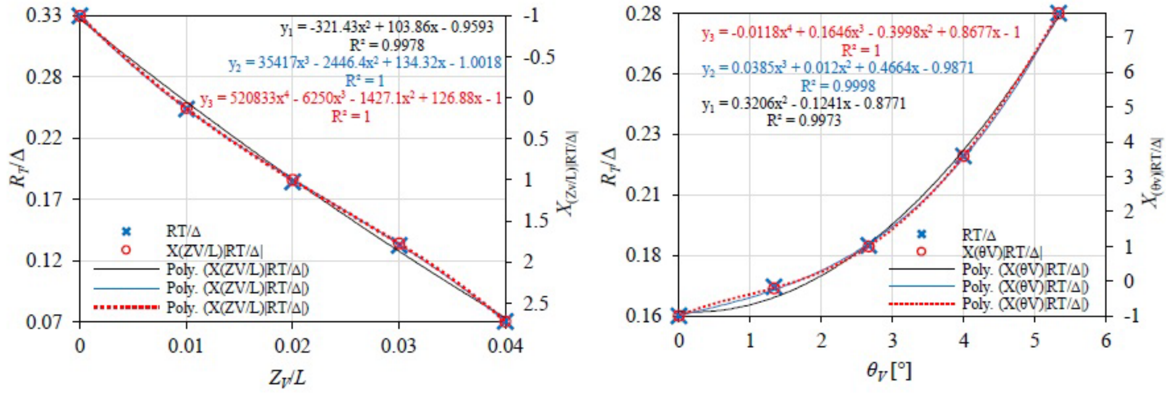

Fig. 12: Non-linear regressions used to determine the equations for the sinkage and trim parameters in relation to the drag response.

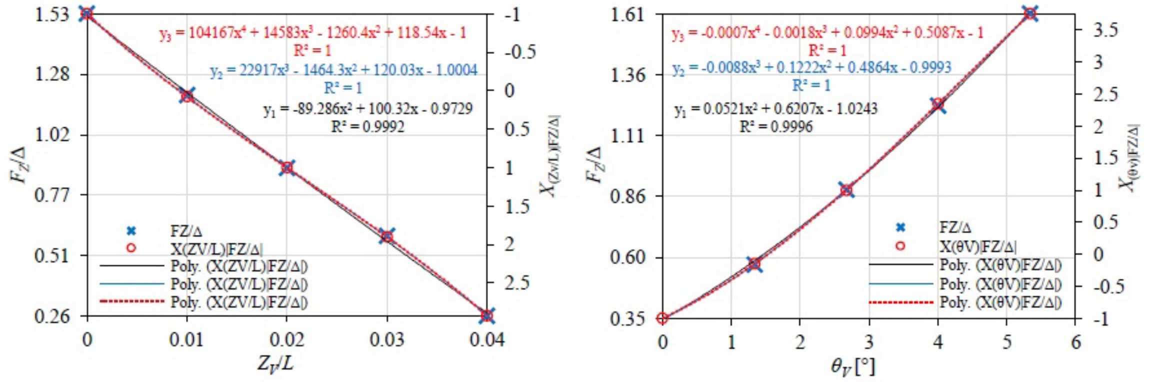

Fig. 13: Employing nonlinear regressions to establish equations for the sinkage and trim parameters concerning the lift response.

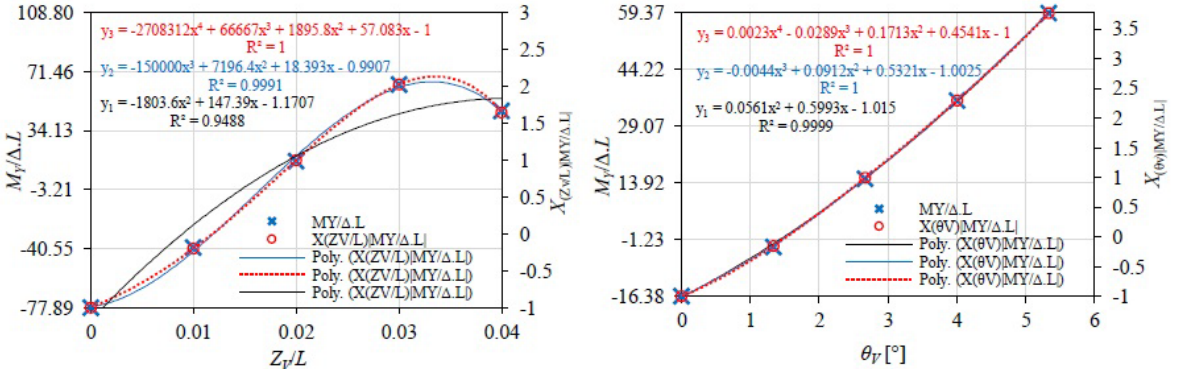

Fig. 14: Utilizing nonlinear regressions to determine the equations with respect to the moment response.

Based on the obtained function matches for each parameter and response, an equation is derived for each parameter weight. The following equation represents the weight of the sinkage parameter (Z_V/L) for the drag response (R_T/Δ) described in Fig. 12 (left), which can be chosen based on order 2 to 4, referred to as y₁, y₂, or y₃. It should be understood that order selection affects value accuracy and computational complexity. Therefore, the equation for obtaining the parameter weight is as follows:

$$X_{\left(\frac{Z_V}{L}\right)_{|R_T/\Delta|}} \rightarrow y_{(\mathrm{n})}(x = Z_V/L) \quad \text{in Fig. 12 left} \tag{42}$$

The equation for the weight of the trim parameter (θ_V) in relation to the drag response (R_T/Δ) is as follows:

$$X_{(\theta_V)_{|R_T/\Delta|}} \rightarrow y_{(\mathrm{n})}(x = \theta_V) \quad \text{in Fig. 12 right} \tag{43}$$

Meanwhile, the equation for the sinkage parameter (Z_V/L) in relation to the lift response (F_Z/Δ) is as follows:

$$X_{\left(\frac{Z_V}{L}\right)_{|F_Z/\Delta|}} \rightarrow y_{(\mathrm{n})}(x = Z_V/L) \quad \text{in Fig. 13 left} \tag{44}$$

The trim (θ_V) parameter weight equation for the lift response (F_Z/Δ) is as follows:

$$X_{(\theta_V)_{|F_Z/\Delta|}} \rightarrow y_{(\mathrm{n})}(x = \theta_V) \quad \text{in Fig. 13 right} \tag{45}$$

For the moment response ($M_Y/(\Delta \cdot L)$), the sinkage parameter (Z_V/L) weight equation is as follows:

$$X_{\left(\frac{Z_V}{L}\right)_{|M_Y/\Delta.L|}} \rightarrow y_{(\mathrm{n})}(x = Z_V/L) \quad \text{in Fig. 14 left} \tag{46}$$

The trim parameter (θ_V) weight equation for the moment ($M_Y/(\Delta \cdot L)$) is as follows:

$$X_{(\theta_V)_{|M_Y/\Delta.L|}} \rightarrow y_{(\mathrm{n})}(x = \theta_V) \quad \text{in Fig. 14 right} \tag{47}$$

3.4.Validation of model equations

Since the three response equations have been successfully formulated, it is now possible to predict the values of drag, lift, and moment based on the sinkage and trim parameters without the need to conduct additional CFD simulations. To forecast the drag (R_T/Δ), a combination of Equations (37), (42) and (43) can be employed. Similarly, the lift (F_Z/Δ) value can be predicted by utilizing the combination of Equations (39), (44), and (45). Moreover, the moment ($M_Y/(\Delta \cdot L)$) can be predicted by applying the combination of Equations (41), (46) and (47).

However, validation must be performed first. Validation is necessary to determine how accurately the predictions from the model equations compare to the CFD simulation results. This validation uses RMSE (root mean square error) calculations as explained in Table 9 to Table 11, and linear regression along with R² (coefficient of determination) values shown in Fig. 15.

The validation results of the three predicted outcomes show that the order 4 function (y_3) is the most accurate, with the highest error among the three models being only 1.23% (see Table 11). The Accuracy is assessed based on the smallest RMSE, as shown in Table 9 to Table 11. The error ($E_{(\psi)}$) is calculated according to Equation (48), and then RMSE is calculated according to Equation (49). Where, ψ_{ME} is the result value from the model equation for R_T/Δ, F_Z/Δ, or $M_Y/\Delta.L$ for each polynomial, and ψ_{CFD} is the result value from the CFD simulation for R_T/Δ, F_Z/Δ, or $M_Y/\Delta.L$.

From the appearance of the linear regression plot results comparing the equation model and CFD results shown in Fig. 15, the equation of order 4 is the best. A perfectly valid value is when y = x + 0 and the coefficient of determination R² = 1. The functions of order 4, or y3, are very close to these ideal conditions. Therefore, it can be concluded that the model response equation accurately represents the CFD simulation results with good accuracy.

Based on the successful validation results of the equation model that has been created, it is no longer necessary to collect data using CFD simulations in order to obtain values of resistance, lift, and moments with different parameter values.

$$E_{(\psi)}\% = \frac{\psi_{ME}-\psi_{CFD}}{\psi_{CFD}} \times 100\% \qquad (48)$$

$$\text{RSME} = \sqrt{\sum_{i=1}^{N} \frac{(E_{\psi}{}^{2})}{N}} \qquad (49)$$

Table 9. The RMSE calculations for the three response equations using a non-linear polynomial function of order 2.

Parameters		**R_T/Δ**			**F_Z/Δ**			**($M_Y/\Delta.L$)**		
Z_V/L	**θ_V [°]**	**CFD**	**Eq. y_1**	**E[%]**	**CFD**	**Eq. y_1**	**E[%]**	**CFD**	**Eq. y_1**	**E[%]**
0	0	0.36	0.36	-1.68	1.03	1.01	-1.48	-76.25	-81.32	6.66
0.02	0	0.16	0.16	1.84	0.35	0.35	-1.60	-16.38	-14.96	-8.69
0	2.67	0.33	0.33	-1.25	1.53	1.53	-0.50	-77.89	-85.78	10.13
0.02	2.67	0.19	0.19	1.01	0.88	0.88	0.21	14.98	17.32	15.65
0.02	1.335	0.17	0.17	-1.93	0.57	0.59	3.00	-3.15	-0.43	-86.31
0.02	4.005	0.22	0.23	1.76	1.23	1.23	-0.15	35.93	38.30	6.60
0.02	5.34	0.28	0.28	0.11	1.61	1.62	0.67	59.38	62.50	5.27
0.01	2.67	0.25	0.25	2.12	1.19	1.20	1.07	-39.97	-25.88	-35.25
0.03	2.67	0.13	0.13	-3.63	0.60	0.57	-3.72	63.35	43.81	-30.84
0.04	2.67	0.07	0.07	4.91	0.26	0.27	3.14	46.57	53.60	15.10
		RMSE = 2.02%			**RMSE = 1.56%**			**RMSE = 22.05%**		

Table 10. The RMSE calculations for the three response equations using a non-linear polynomial function of order 3.

Parameters		**R_T/Δ**			**F_Z/Δ**			**($M_Y/\Delta.L$)**		
Z_V/L	**θ_V [°]**	**CFD**	**Eq. y_2**	**E[%]**	**CFD**	**Eq. y_2**	**E[%]**	**CFD**	**Eq. y_2**	**E[%]**
0	0	0.36	0.36	-0.01	1.03	1.03	0.03	-76.25	-75.97	-0.37
0.02	0	0.16	0.16	0.81	0.35	0.35	0.26	-16.38	-14.75	-9.94
0	2.67	0.33	0.33	-0.34	1.53	1.53	0.06	-77.89	-77.45	-0.57
0.02	2.67	0.19	0.19	1.00	0.88	0.88	0.17	14.98	17.32	15.62
0.02	1.335	0.17	0.17	-0.03	0.57	0.58	0.68	-3.15	-0.83	-73.52
0.02	4.005	0.22	0.22	0.31	1.23	1.24	0.84	35.93	38.68	7.67
0.02	5.34	0.28	0.29	0.66	1.61	1.61	0.12	59.38	62.26	4.85
0.01	2.67	0.25	0.25	-0.26	1.19	1.18	-0.46	-39.97	-42.55	6.47
0.03	2.67	0.13	0.13	0.86	0.60	0.59	-0.78	63.35	60.48	-4.53
0.04	2.67	0.07	0.07	0.41	0.26	0.26	-0.46	46.57	45.26	-2.81
		RMSE = 0.47%			**RMSE = 0.39%**			**RMSE = 12.63%**		

Table 11. The RMSE calculations for the three response equations using a non-linear polynomial function of order 4.

Parameters		**R_T/Δ**			**F_Z/Δ**			**($M_Y/\Delta.L$)**		
Z_V/L	**θ_V [°]**	**CFD**	**Eq. y_3**	**E[%]**	**CFD**	**Eq. y_3**	**E[%]**	**CFD**	**Eq. y_3**	**E[%]**
0	0	0.36	0.36	0.00	1.03	1.03	0.00	-76.25	-76.25	0.00
0.02	0	0.16	0.16	-0.01	0.35	0.35	0.00	-16.38	-16.38	0.00
0	2.67	0.33	0.33	0.00	1.53	1.53	-0.05	-77.89	-77.89	0.00
0.02	2.67	0.19	0.19	0.00	0.88	0.88	-0.09	14.98	14.98	0.04
0.02	1.335	0.17	0.17	-0.15	0.57	0.58	0.69	-3.15	-3.05	-3.19
0.02	4.005	0.22	0.23	0.51	1.23	1.24	0.62	35.93	35.38	-1.52
0.02	5.34	0.28	0.29	0.75	1.61	1.60	-0.50	59.38	58.55	-1.40
0.01	2.67	0.25	0.25	-0.10	1.19	1.18	-0.55	-39.97	-40.74	1.94
0.03	2.67	0.13	0.13	-0.31	0.60	0.59	-0.97	63.35	62.58	-1.21
0.04	2.67	0.07	0.06	-4.52	0.26	0.26	-1.14	46.57	45.17	-3.01
		RMSE = 0.64%			**RMSE = 0.46%**			**RMSE = 1.23%**		

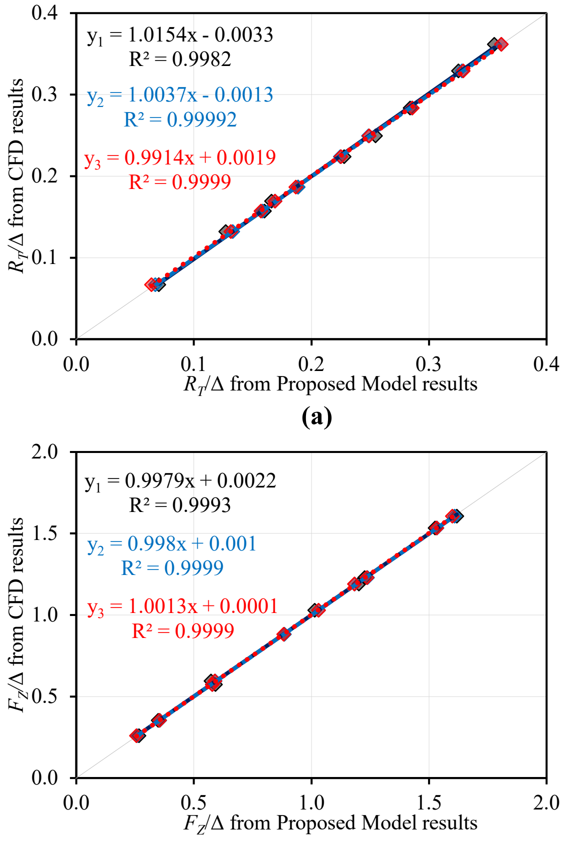

(a)

(b)

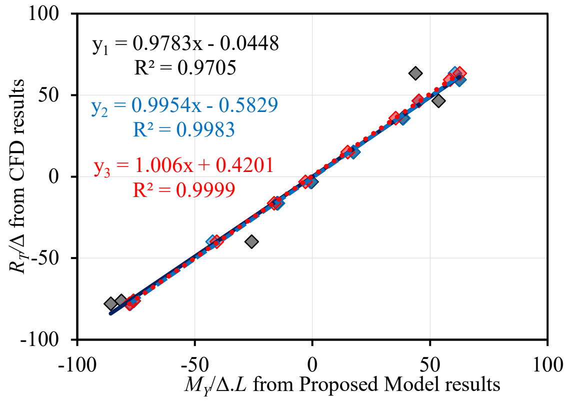

(c)

Fig. 15: Comparing the predicted outcomes for the three responses using the developed model against the CFD results, where: (a) total resistance, (b) sinkage, and (c) trim.

3.5.Weight variations sensitivity analysis

At this stage, the differences in resistance, trim, and sinkage of the ship resulting from changes in its weight and center of gravity were analyzed. The change in weight value or displacement is represented by the symbol A%, where their values are tabulated in Table 12. Meanwhile, the change in the center of gravity is symbolized by B%, and their values are tabulated in Table 13. Each of these variations interacts and influences each other, leading to predicted changes in resistance, trim, and sinkage values. The prediction calculation method utilizes an optimization approach explained in Subsection 2.3, where the trim (θ_V) and sinkage (Z_V/L) values are iterated to obtain a new resistance value while considering the specified boundary conditions. These boundary conditions are determined based on the equilibrium of forces ($\sum F_Z = 0$) and moments ($\sum M_Y = 0$).

Table 12 Variations in weight value adjustments.

A%	δΔ (N)	Δ (N)
-10	-24.5	220.37
-5	-12.2	232.61
0	0.0	244.86
+5	+12.2	257.10
+10	+24.5	269.34

Table 13 Variations in the changes of the center of gravity location.

B%	B (m)	LCG%	LCG (m)
-2.25	-0.045	30.75	0.615
---	---	---	---
0	0	33	0.66
---	---		
+2.00	0.04	35	0.7

3.5.1. Variation in Performance Compared to the Initial Design

The calculation results of the new resistance (R_T/Δ_0) and its changes ($\delta(R_T/\Delta_0)$) compared to the initial resistance value are explained here. The initial conditions where $A = 0\%$ and $B = 0\%$, with the parameters as described in Table 1, where Δ_0 = 244.84 N and l_{CG} = 33%L. These initial conditions produced a resistance per displacement, R_T/Δ_0= 0.1867. All prediction results are presented in the form of curves displayed in the form of curves displayed in Fig. 16 and with a detailed zoom-in provided in Fig. 17.

The prediction results indicate that alterations in weight have a significant influence on the resistance experienced by the ship. It is observed that as the weight of the ship increases, the resistance correspondingly increases. This relationship is clearly depicted by the upward trend observed in the yellow line (representing a weight increase of 5%) and the steeper increase depicted by the purple line (representing a weight increase of 10%). On the other hand, when the cargo is reduced, the ship's resistance diminishes. This inverse relationship is evident from the downward trend observed in the green line (representing a weight reduction of 5%) and the more substantial decrease portrayed by the blue line (representing a weight reduction of 10%). These findings highlight the critical role that weight variations play in influencing the resistance encountered by the ship.

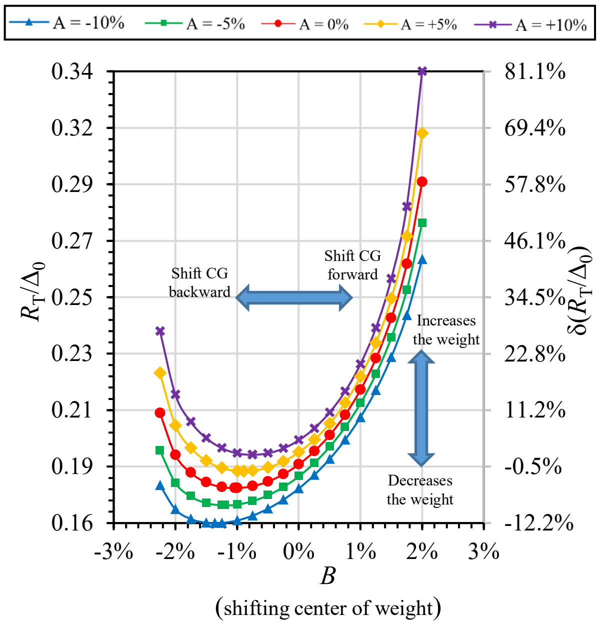

Fig. 16: The predicted resistance (y-axis) resulting from alterations in weight (denoted as A, with 5 different colored curves) and center of gravity (B on the x-axis), compared to the initial design's weight and center of gravity.

The prediction results show that variations in the location of the center of gravity produce different resistance values. This relationship is illustrated by a characteristic curve that resembles inverted parabolical curves, indicating that there is a minimum value. Fig. **17** provides a visual representation of this phenomenon, where the red line ($A = 0\%$) represents no change in the amount of weight. Remarkably, by shifting the position of the center of gravity backwards by about 1%, the ship's drag is reduced by up to 5%. On the contrary, if the center of gravity is shifted forward by about 1%, an unfortunate consequence is observed—resistance increases by up to 15%.

The unique finding is that the drag does not change when the weight is increased by 5%, as long as the center of gravity is shifted back by about 0.5%. Moreover, when the center of gravity is shifted to -1%, the resistance actually decreases to around 2%. The uniqueness of this lies in the fact that increasing the weight of the payload does not always increase drag. As long as the center of gravity is in a suitable location, the ship's performance can be improved. These findings highlight the importance of carefully managing weight and center of gravity to optimize ship performance. By strategically adjusting the cargo load and precisely positioning the center of gravity, it is possible to achieve a balance that minimizes drag and increases the ship's overall efficiency.

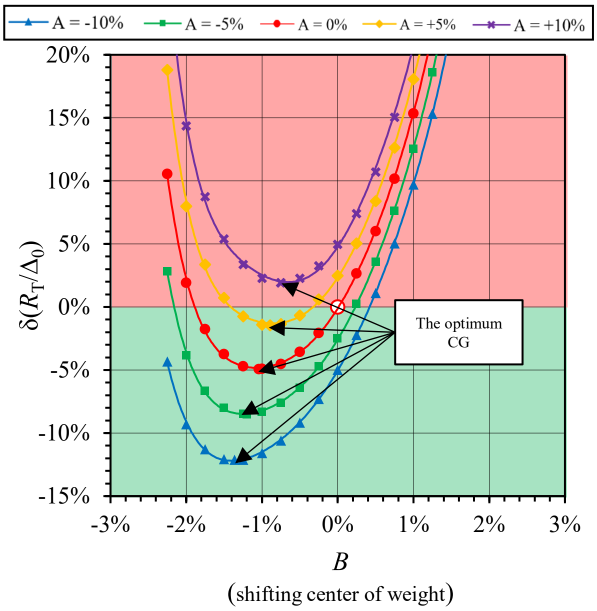

Fig. 17: An enlarged detail from Fig. 16 reveals that the green area effectively reduces resistance, whereas the red area, in contrast, contributes to an increase in resistance.

3.5.2. Variation in Performance Compared to the Current Design

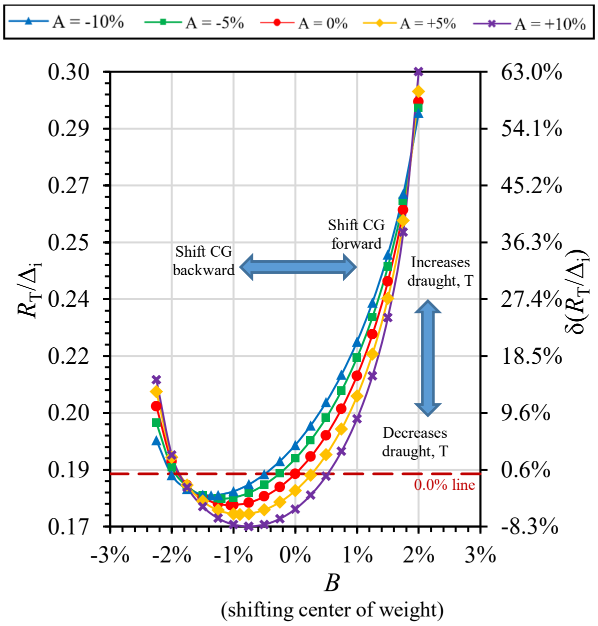

Fig. 18: The predicted performance resulting from variations in weight (denoted as A, with 5 different colored curves) and center of gravity (*B* on the x-axis), in comparison to the performance of the initial design.

This chapter will discuss the performance changes resulting from variations in weight and center of gravity of the ship, with different performance evaluations. Performance here refers to the resistance force of the ship and its ability to carry cargo. The difference from the previous subsection is the change in resistance compared to the initial design, denoted as R_T/Δ_0, where Δ_0 represents the weight value of the ship according to Table 1 and can be found in Equation (12). Whereas in this sub-chapter, the change in resistance value per displacement is compared to the initial design formulated in Equation (13), denoted as R_T/Δ_i, where $\Delta_i = \Delta_0(1+A\%)$. The prediction outcomes are depicted as curves in Fig. 18, while Fig. **19** offers a close-up view with more detailed information.

Based on the findings depicted in Fig. 18 and Fig. 19, it becomes apparent that variations in weight and center of gravity contribute to significant differences in performance. Notably, when the weight change ($A\%$) is augmented by 10% (as illustrated by the purple line), and the center of gravity ($B\%$) is carefully adjusted to its optimal position, approximately -0.8%, the resultant value demonstrates a notably enhanced performance (R_T/Δ_i) in comparison to the original design configuration. This improvement in performance amounts to an approximate increase of 8.26%.

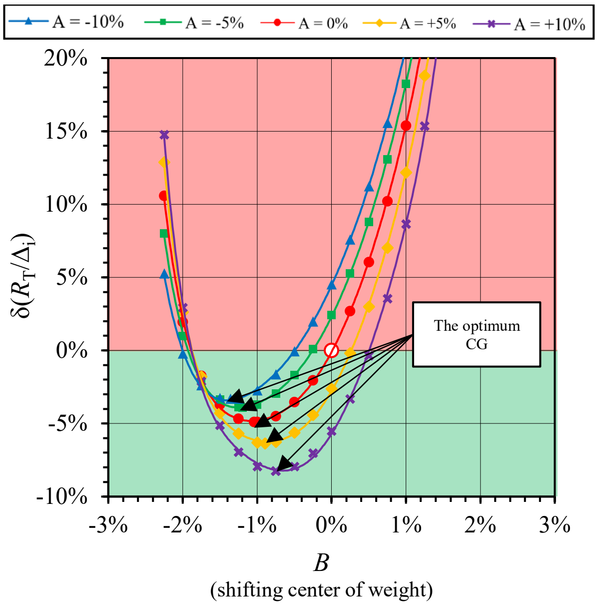

Fig. 19: An enlarged detail from Fig. 18 reveals that the green area effectively enhances performance, whereas the red area, in contrast, leads to a decrease in performance.

3.5.3. Change in sinkage and trim motions

In this sub-chapter, the predicted results of sinkage and trim values due to variations in changes in weight and center of gravity are explained. The sinkage and trim values, which represent the dynamic draught at which a vessel submerges in the water, were examined based on variations in weight and the center of gravity. Fig. **20** illustrates the predicted results of sinkage values, while Fig. **21** provides insights into the trim values, which refer to the longitudinal balance of the vessel.

The results of the analysis explain that the center of gravity plays a dominant role in influencing changes in sinkage and trim values. When the center of gravity is shifted towards the rear of the vessel, both the sinkage value and trim increase. This means that the vessel will submerge deeper into the water and have a higher inclination at the stern. On the other hand, shifting the center of gravity towards the front leads to a decrease in both the sinkage and trim values. Consequently, the vessel will experience less submergence and exhibit a more level orientation.

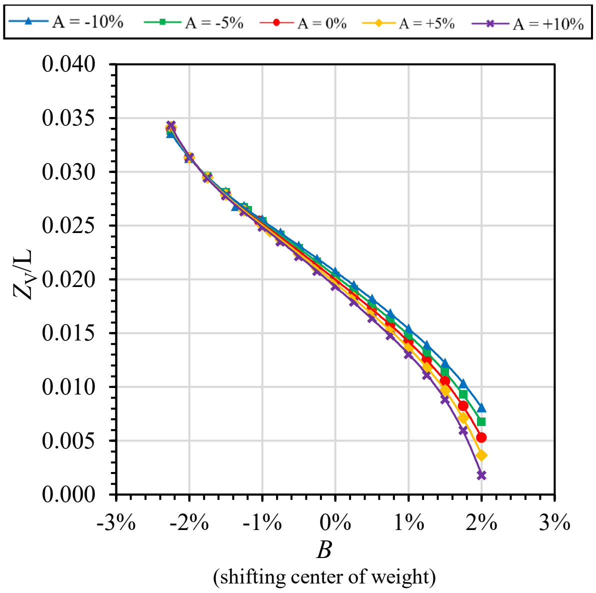

Fig. 20: Prediction results of sinkage values resulting from variations in weight and center of gravity.

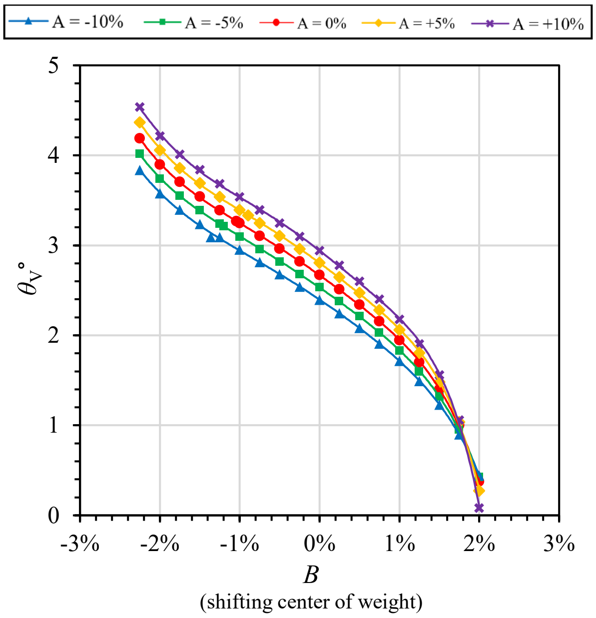

Fig. 21: Prediction results of trim values resulting from variations in weight and center of gravity.

The impact of weight changes on sinkage and trim changes is also analyzed. It is observed that weight variations have a significant influence on the trim, except when the center of gravity is shifted forward from 1.5% to 2%. Alterations in weight result in a relatively moderate change in the sinkage value when the center of gravity shifts from -2.25% to approximately 0.5%. However, the effect becomes more pronounced as the center of gravity further shifts from 0.5% to 2%.

4. Conclusions

This study utilizes various methodologies to minimize drag on a high-speed boat with a planing hull, achieved by optimizing weight and center of gravity variations. The optimization method is crucial for identifying the optimal drag reduction value based on sinkage and trim parameters while adhering to prescribed limit conditions for force and moment equilibrium. The objective equation is formulated using Design of Experiments (DOE) and Response Surface Methodology (RSM) techniques, utilizing data from verified and validated Computational Fluid Dynamics (CFD) simulations. The objective equation has undergone validation and meets the necessary criteria.

Predictive results reveal that modifications in weight exert a substantial impact on the resistance encountered by the boat. The observed trend indicates that an increase in the boat's weight corresponds to a proportional increase in resistance. Conversely, a reduction in cargo results in a decrease in the boat's resistance, underscoring the pivotal role of weight variations in influencing the resistance experienced by the boat. The predictive outcomes indicate that alterations in the center of gravity's position result in distinct resistance values for the boat. This association is depicted by a characteristic curve with an inverted parabolic shape, suggesting the presence of a minimum value. By moving the center of gravity backward by approximately 1%, the boat's drag was reduced by up to 5%, while a forward shift in the center of gravity by about 1% led to an increase in resistance by up to 15%.

A noteworthy discovery is that the boat's resistance remains constant when the weight is increased by 5%, provided the center of gravity is shifted backward by approximately -0.5%. Additionally, when the center of gravity is shifted to -1%, the resistance decreases to around 2%. This observation highlights the importance of appropriately positioning the center of gravity to enhance the boat's performance. The data analysis reveals a significant influence of the center of gravity on the sinkage and trim values of the vessel. Shifting the center of gravity towards the rear increases both sinkage and trim, leading to deeper submergence and a higher inclination at the stern. Conversely, relocating the center of gravity towards the front reduces sinkage and trim, resulting in less submergence and a more level orientation.

The importance of a tailored approach in optimizing weight and the center of gravity for different ship hulls is underlined, considering the unique characteristics and performance requirements of each ship. Through the utilization of appropriate methodologies and consideration of individual hull attributes, improvements in the efficiency and performance of various ship designs can be achieved. While attempting to reduce the drag of fast ships, which will result in a reduction in energy consumption and emissions, even a modest reduction can have a significant impact on benefits, especially with a very large fleet.

Acknowledgements

This research was supported by the Institute for Research and Community Services (LPPM), Universitas Diponegoro, Indonesia, through the Riset Publikasi Internasional (RPI) 2023 as a research funding scheme with contract number 609-104/UN7.D2/PP/VIII/2023.

References

1) IMO, “Fourth Greenhouse Gas Study 2020,” 2020.
2) H. Huzaifi, A. Budiyanto, and J. Sirait, “Study on the carbon emission evaluation in a container port based on energy consumption data,” *Evergreen*, **7** (*1*) 97–103 (2020). doi:10.5109/2740964.
3) Intergovernmental Panel on Climate Change, “Climate Change and Land,” Cambridge University Press, 2022. doi:10.1017/9781009157988.
4) M.K. Barai, and B.B. Saha, “Energy security and sustainability in japan,” *Evergreen*, **2** (*1*) 49–56 (2015). doi:10.5109/1500427.
5) N. Bhasin, R.N. Kar, and N. Arora, “Green disclosure practices in india : a study of select companies,” *Evergreen*, **2** (*2*) 5–13 (2015). doi:10.5109/1544075.
6) Y. Sugimura, T. Kawasaki, and S. Murakami, “Potential for increased use of secondary raw materials in the copper industry as a countermeasure against climate change in japan,” *Sustainable Production and Consumption*, **35** 275–286 (2023). doi:10.1016/j.spc.2022.11.007.
7) H. Wang, and N. Lutsey, “Long-term potential to reduce emissions from international shipping by adoption of best energy-efficiency practices,” *Transportation Research Record*, **2426** 1–10 (2014). doi:10.3141/2426-01.
8) Abdelgader A.S. Gheidan, Mazlan Bin Abdul Wahid, Opia A. Chukwunonso, and Mohd Fairus Yasin, “Impact of internal combustion engine on energy supplyand its emission reduction via sustainable fuel source,” *Evergreen*, **9** (*3*) 830–844 (2022). doi:10.5109/4843114.
9) IMO, “International convention for the prevention of pollution from ships,” *MARPOL Convention Outline*, (1973).
10) P. Serra, and G. Fancello, “Towards the imo’s ghg goals: a critical overview of the perspectives and challenges of the main options for decarbonizing international shipping,” *Sustainability*, **12** (*8*) 3220 (2020). doi:10.3390/su12083220.
11) ICCT, “Reducing greenhouse gas emissions from ships,” *White Paper*, (*11*) (2011).
12) A.F. Molland, S.R. Turnock, D.A. Hudson, and I.K.A.P. Utama, “Reducing ship emissions: a review of potential practical improvements in the propulsive efficiency of future ships,” *Transactions of the Royal Institution of Naval Architects Part A: International Journal of Maritime Engineering*, **156** (*PART A2*)

175–188 (2014). doi:10.3940/rina.ijme.2014.a2.289.

13) T. Tuswan, D.P. Sari, T. Muttaqie, A.R. Prabowo, M. Soetardjo, T.T.P. Murwantono, R. Utina, and Y. Yuniati, "Representative application of lng-fuelled ships: a critical overview on potential ghg emission reductions and economic benefits," *Brodogradnja*, **74** (*1*) 63–83 (2023). doi:10.21278/brod74104.

14) D.P. Sari, T. Tuswan, T. Muttaqie, M. Soetardjo, T.T.P. Murwatono, R. Utina, Y. Yuniati, Aditya Rio Prabowo, and S. Misbahudin, "Critical overview and challenge of representative lng-fuelled ships on potential ghg emission reduction," *Evergreen*, **10** (*3*) 1792–1808 (2023). doi:10.5109/7151729.

15) A. Arteconi, C. Brandoni, D. Evangelista, and F. Polonara, "Life-cycle greenhouse gas analysis of lng as a heavy vehicle fuel in europe," *Applied Energy*, **87** (*6*) 2005–2013 (2010). doi:10.1016/j.apenergy.2009.11.012.

16) Z. Wang, Y. Wang, S. Afshan, and J. Hjalmarsson, "A review of metallic tanks for h2 storage with a view to application in future green shipping," *International Journal of Hydrogen Energy*, **46** (*9*) 6151–6179 (2021). doi:10.1016/j.ijhydene.2020.11.168.

17) K. Kim, G. Roh, W. Kim, and K. Chun, "A preliminary study on an alternative ship propulsion system fueled by ammonia: environmental and economic assessments," *Journal of Marine Science and Engineering*, **8** (*3*) 183 (2020). doi:10.3390/jmse8030183.

18) N.A. Lestari, "Reduction of co_2 emission by integrated biomass gasification-solid oxide fuel cell combined with heat recovery and in-situ co_2 utilization," *Evergreen*, **6** (*3*) 254–261 (2019). doi:10.5109/2349302.

19) C. Nuchturee, T. Li, and H. Xia, "Energy efficiency of integrated electric propulsion for ships – a review," *Renewable and Sustainable Energy Reviews*, **134** 110145 (2020). doi:10.1016/j.rser.2020.110145.

20) M. Motinur Rahman, S. Saha, M. Z. H. Majumder, T. Tamrin Suki, M. Habibur Rahman, F. Akter, M. A. S. Haque, and M. Khalid Hossain, "Energy conservation of smart grid system using voltage reduction technique and its challenges," *Evergreen*, **9** (*4*) 924–938 (2022). doi:10.5109/6622879.

21) V. Trivedi, A. Saxena, M. Javed, P. Kumar, and V. Singh, "Design of six seater electrical vehicle (golf cart)," *Evergreen*, **10** (*2*) 953–961 (2023). doi:10.5109/6792890.

22) A. Nasirudin, H. Hasanudin, D. Utama, and L.P. Tahwoto, "Determination of pv power and battery capacity size for a leisure solar powered boat at kalimas river, surabaya, indonesia," *Kapal: Jurnal Ilmu Pengetahuan Dan Teknologi Kelautan*, **17** (*3*) 123–129 (2020). doi:10.14710/kapal.v17i3.31965.

23) S. Sunaryo, and F. Yusro, "Hull design of solar powered recreational electric boat for indonesian waters," *E3S Web of Conferences*, **67** 03010 (2018). doi:10.1051/e3sconf/20186703010.

24) J. He, Y. Hu, J. Tang, and S. Xue, "Research on sail aerodynamics performance and sail-assisted ship stability," *Journal of Wind Engineering and Industrial Aerodynamics*, **146** 81–89 (2015). doi:10.1016/j.jweia.2015.08.005.

25) N. Bigi, K. Roncin, J.-B. Leroux, and Y. Parlier, "Ship towed by kite: investigation of the dynamic coupling," *Journal of Marine Science and Engineering*, **8** (*7*) 486 (2020). doi:10.3390/jmse8070486.

26) B. Taskar, and P. Andersen, "Benefit of speed reduction for ships in different weather conditions," *Transportation Research Part D: Transport and Environment*, **85** 102337 (2020). doi:10.1016/j.trd.2020.102337.

27) R. Leaper, "The role of slower vessel speeds in reducing greenhouse gas emissions, underwater noise and collision risk to whales," *Frontiers in Marine Science*, **6** (2019). doi:10.3389/fmars.2019.00505.

28) N.R. Ammar, "Energy- and cost-efficiency analysis of greenhouse gas emission reduction using slow steaming of ships: case study ro-ro cargo vessel," *Ships and Offshore Structures*, **13** (*8*) 868–876 (2018). doi:10.1080/17445302.2018.1470920.

29) T.P.V. Zis, H.N. Psaraftis, and L. Ding, "Ship weather routing: a taxonomy and survey," *Ocean Engineering*, **213** 107697 (2020). doi:10.1016/j.oceaneng.2020.107697.

30) N. Degiuli, A. Farkas, I. Martić, and C.G. Grlj, "Optimization of maintenance schedule for containerships sailing in the adriatic sea," *Journal of Marine Science and Engineering*, **11** (*1*) 201 (2023). doi:10.3390/jmse11010201.

31) M.P. Schultz, J.A. Bendick, E.R. Holm, and W.M. Hertel, "Economic impact of biofouling on a naval surface ship," *Biofouling*, **27** (*1*) 87–98 (2011). doi:10.1080/08927014.2010.542809.

32) M.L. Hakim, I.K. Suastika, and I.K.A.P. Utama, "A practical empirical formula for the calculation of ship added friction-resistance due to (bio)fouling," *Ocean Engineering*, **271** 113744 (2023). doi:10.1016/j.oceaneng.2023.113744.

33) M.L. Hakim, B. Nugroho, I.K. Suastika, and I.K.A.P. Utama, "Alternative empirical formula for predicting the frictional drag penalty due to fouling on the ship hull using the design of experiments (doe) method," *International Journal of Technology*, **12** (*4*) 829 (2021). doi:10.14716/ijtech.v12i4.4692.

34) I.K.A.P. Utama, B. Nugroho, M. Yusuf, F.A. Prasetyo, M.L. Hakim, I.K. Suastika, B. Ganapathisubramani, N. Hutchins, and J.P. Monty, "The effect of cleaning and repainting on the ship drag penalty," *Biofouling*, **37** (*4*) 372–386 (2021). doi:10.1080/08927014.2021.1914599.

35) M.L. Hakim, B. Nugroho, T. Putranto, K. Suastika, and I.K.A.P. Utama, "Assessment of Drag Penalty Resulting from The Roughness of Freshly Cleaned and Painted Ship-Hull Using Computational FLuid Dynamics," in: 11st International Conference on Marine Technology MARTEC 2018, mtc-utm.my, Kuala Lumpur, Malaysia, 2018.

36) M.L. Hakim, and T. Yulianto, "Stresses Comparative Analysis Between Hull-V and Hull-U due to Slamming Pressure using Finite Element Method," in: SENTA: Seminar Nasional Teori Dan Aplikasi Teknologi Kelautan, Surabaya, Indonesia, 2015: pp. X39-46.

37) S. Song, Y.K. Demirel, and M. Atlar, "Penalty of hull and propeller fouling on ship self-propulsion performance," *Applied Ocean Research*, **94** 102006 (2020). doi:10.1016/j.apor.2019.102006.

38) J. Comas, D. Parra, J.C. Balasch, and L. Tort, "Effects of fouling management and net coating strategies on reared gilthead sea bream juveniles," *Animals*, **11** (*3*) (2021). doi:10.3390/ani11030734.

39) L. Tian, Y. Yin, W. Bing, and E. Jin, "Antifouling technology trends in marine environmental protection," *Journal of Bionic Engineering*, **18** (*2*) 239–263 (2021). doi:10.1007/s42235-021-0017-z.

40) H. Yan, Q. Wu, C. Yu, T. Zhao, and M. Liu, "Recent progress of biomimetic antifouling surfaces in marine," *Advanced Materials Interfaces*, 2000966 (2020). doi:10.1002/admi.202000966.

41) K.A. Dafforn, J.A. Lewis, and E.L. Johnston, "Antifouling strategies: history and regulation, ecological impacts and mitigation," *Marine Pollution Bulletin*, **62** (*3*) 453–465 (2011). doi:10.1016/j.marpolbul.2011.01.012.

42) D. Villa, S. Gaggero, G. Tani, and M. Viviani, "Numerical and experimental comparison of ducted and non-ducted propellers," *Journal of Marine Science and Engineering*, **8** (*4*) 257 (2020). doi:10.3390/jmse8040257.

43) Q. Zhang, and R.K. Jaiman, "Numerical analysis on the wake dynamics of a ducted propeller," *Ocean Engineering*, **171** 202–224 (2019). doi:10.1016/j.oceaneng.2018.10.031.

44) S. Nayak, and M. Prasanna Kumar, "Mechanical characterization and static analysis of natural fiber based composite propeller blade," *Evergreen*, **10** (*2*) 805–812 (2023). doi:10.5109/6792832.

45) B.A. Adietya, I.K.A.P. Utama, W.D.A. Aryawan, and S. Sutiyo, "CFD analysis into the effect of using propeller boss cap fins (pbcf) on open and ducted propellers, case study with propeller b-series and kaplan-series," *CFD Letters*, **14** (*4*) 32–42 (2022). doi:10.37934/cfdl.14.4.3242.

46) K. Mizzi, Y.K. Demirel, C. Banks, O. Turan, P. Kaklis, and M. Atlar, "Design optimisation of propeller boss cap fins for enhanced propeller performance," *Applied Ocean Research*, **62** 210–222 (2017). doi:10.1016/j.apor.2016.12.006.

47) I.A.C. Abar, and I.K.A.P. Utama, "Effect of the incline angle of propeller boss cap fins (pbcf) on ship propeller performance," *International Journal of Technology*, **10** (*5*) 1056 (2019). doi:10.14716/ijtech.v10i5.2256.

48) H. Ghassemi, A. Mardan, and A. Ardeshir, "Numerical analysis of hub effect on hydrodynamic performance of propellers with inclusion of pbcf to equalize the induced velocity," *Polish Maritime Research*, **19** (*2*) 17–24 (2012). doi:10.2478/v10012-012-0010-x.

49) M. Mansoori, and A.C. Fernandes, "Interceptor and trim tab combination to prevent interceptor's unfit effects," *Ocean Engineering*, **134** 140–156 (2017). doi:10.1016/j.oceaneng.2017.02.024.

50) S. Samuel, O. Mursid, S. Yulianti, Kiryanto, and M. Iqbal, "Evaluation of interceptor design to reduce drag on planing hull," *Brodogradnja*, **73** (*3*) 93–110 (2022). doi:10.21278/brod73306.

51) M.F. Syahrudin, M.A. Budiyanto, and M.A. Murdianto, "Analysis of the use of stern foil on the high speed patrol boat on full draft condition," *Evergreen*, **7** (*2*) 262–267 (2020). doi:10.5109/4055230.

52) M.L. Hakim, D. Purnamasari, M. Muryadin, F.M. Noor, P. Virliani, E. Suwarni, R. Rina, N. Nurcholid, and R.D.S. Wijaya, "Using trim control to improve energy efficiency on high-speed marine vehicles (hsmv): a review," *EVERGREEN Joint Journal of Novel Carbon Resource Sciences & Green Asia Strategy*, **10** (*03*) 1603–1615 (2023). doi:10.5109/7151709

53) Y. Kodama, A. Kakugawa, T. Takahashi, and H. Kawashima, "Experimental study on microbubbles and their applicability to ships for skin friction reduction," *International Journal of Heat and Fluid Flow*, **21** (*5*) 582–588 (2000). doi:10.1016/S0142-727X(00)00048-5.

54) H. Blattmann, and R. Mülhaupt, "Multifunctional poss cyclic carbonates and non-isocyanate polyhydroxyurethane hybrid materials," *Macromolecules*, **49** (*3*) 742–751 (2016). doi:10.1021/acs.macromol.5b02560.

55) S. Verma, S. Mohanty, and S.K. Nayak, "A review on protective polymeric coatings for marine applications," *Journal of Coatings Technology and Research*, **16** (*2*) 307–338 (2019). doi:10.1007/s11998-018-00174-2.

56) A.S. Khanna, V. Kasturi, and P. Grover, "Development of Superfine Nano-Composites Antifouling Coatings for Ship Hulls," in: Ceramic Transactions, 2017: pp. 425–442. doi:10.1002/9781119407270.ch40.

57) M.L. Hakim, T. Tuswan, A. Firdaus, and O. Mursid, "Investigating the comparison of ship resistance components between u and v-shaped hulls," *Jurnal*

Teknologi, **85** (*3*) 153–164 (2023). doi:10.11113/jurnalteknologi.v85.19382.

58) A. Trimulyono, M.L. Hakim, C. Ardhan, S.T.P. Ahmad, T. Tuswan, and A.W.B. Santosa, "Analysis of the double steps position effect on planing hull performances," *Brodogradnja*, **74** (*4*) 41–72 (2023). doi:10.21278/brod74403.
59) M.L. Hakim, I.K. Suastika, I.K.A.P. Utama, D. Purnamasari, and M. Muryadin, "Frictional resistance increase due to hull roughness: an analysis of the hull form parameters influence," *Transactions on Maritime Science*, **12** (*2*) (2023). doi:10.7225/toms.v12.n02.002.
60) E. Sugianto, J.-H. Chen, and N.V.A. Permadi, "Effect of monohull type and catamaran hull type on ocean waste collection behavior using openfoam," *Water*, **14** (*17*) 2623 (2022). doi:10.3390/w14172623.
61) E. Sugianto, J. Horng-Chen, and N.P. Purba, "Numerical investigation of conveyor wing shape type effect on ocean waste collection behavior," *E3S Web of Conferences*, **324** 01005 (2021). doi:10.1051/e3sconf/202132401005.
62) G. Bangga, A. Ashfahani, E. Sugianto, D. Sa'adiyah, T. Putri, E. Jost, and T. Lutz, "Three-dimensional flow in the vicinity of a circular cylinder mounted to a flat plate at high Reynolds number," in: AIP Conference Proceedings, 2017: p. 030012. doi:10.1063/1.4968265.
63) L.J. Doctors, "Hydrodynamics of High-speed Small Craft," Department of Naval Engineering and Marine Engineering, The University of Michigan, Michigan, 1985.
64) O.M. Faltinsen, "Hydrodynamics of High-Speed Marine Vehicles," Cambridge University Press, 2006. doi:10.1017/CBO9780511546068.
65) O.F. Hughes, T.R. McNatt, and B.J. Spradbrow, "Structural Design of Large, Fast Marine Vehicles Based on First Principles.," in: 1993. https://api.semanticscholar.org/CorpusID:106469340.
66) R.K. Nangia, "Aerodynamic and hydrodynamic aspects of high-speed water surface craft," *The Aeronautical Journal*, **91** (*906*) 241–268 (1987). doi:10.1017/S0001924000021345.
67) T.G. Tran, Q. Van Huynh, and H.C. Kim, "Optimization strategy for planing hull design," *International Journal of Naval Architecture and Ocean Engineering*, **14** 100471 (2022). doi:10.1016/j.ijnaoe.2022.100471.
68) G. Fridsma, "A Systematic Study of the Rough-water Performance of Planing Boats," 1969. http://resolver.tudelft.nl/uuid:75b17497-038c-4266-b844-36f89a38319f.
69) A.G. Avci, and B. Barlas, "An experimental investigation of interceptors for a high speed hull," *International Journal of Naval Architecture and Ocean Engineering*, **11** (*1*) 256–273 (2019). doi:10.1016/j.ijnaoe.2018.05.001.
70) O.S. Sahin, E. Kahramanoglu, and F. Cakici, "Numerical evaluation on the effects of interceptor layout and blade heights for a prismatic planing hull," *Applied Ocean Research*, **127** 103302 (2022). doi:10.1016/j.apor.2022.103302.
71) J.-Y. Park, H. Choi, J. Lee, H. Choi, J. Woo, S. Kim, D.J. Kim, S.Y. Kim, and N. Kim, "An experimental study on vertical motion control of a high-speed planing vessel using a controllable interceptor in waves," *Ocean Engineering*, **173** 841–850 (2019). doi:10.1016/j.oceaneng.2019.01.019.
72) P. Ghadimi, A. Loni, H. Nowruzi, A. Dashtimanesh, and S. Tavakoli, "Parametric study of the effects of trim tabs on running trim and resistance of planing hulls," *Advanced Shipping and Ocean Engineering*, **3** (*1*) 1–12 (2014).
73) A. Fitriadhy, L.Y. Pheng, I.N.H. Adzkh, F. Mahmuddin, A.A. Bakar, M.A. Musa, and M.S. Sulaiman, "Computational investigation of pitch motion of a high-speed craft incorporated with trim-tabs," *CFD Letters*, **14** (*6*) 56–71 (2022). doi:10.37934/cfdl.14.6.5671.
74) T. Celano, "The prediction of porpoising inception for modern planing craft," *SNAME Transactions*, **106** 269–92 (1998).
75) K. Suastika, A. Hidayat, and S. Riyadi, "Effects of the application of a stern foil on ship resistance: a case study of an orela crew boat," *International Journal of Technology*, **8** (*7*) 1266 (2017). doi:10.14716/ijtech.v8i7.691.
76) H. Sun, and O.M. Faltinsen, "The influence of gravity on the performance of planing vessels in calm water," *Journal of Engineering Mathematics*, **58** (*1–4*) 91–107 (2007). doi:10.1007/s10665-006-9107-5.
77) M.F. Islam, and L.M. Lye, "Combined use of dimensional analysis and modern experimental design methodologies in hydrodynamics experiments," *Ocean Engineering*, **36** 237–247 (2009). doi:10.1016/j.oceaneng.2008.11.004.
78) L.M. Lye, "Design of experiments in civil engineering: Are we still in the 1920'S?," in: Proceedings, Annual Conference - Canadian Society for Civil Engineering, Montreal, Canada, 2002.
79) K. Kazemi, B. Zhang, L.M. Lye, Q. Cai, and T. Cao, "Design of experiment (doe) based screening of factors affecting municipal solid waste (msw) composting," *Waste Management*, (2016). doi:10.1016/j.wasman.2016.08.029.
80) A. Chandra, A. Yadav, S. Singh, and Pawan Kumar Arora, "Optimisation of machining parameters for cnc milling of fibre reinforced polymers," *Evergreen*, **10** (*2*) 765–773 (2023). doi:10.5109/6792826.
81) V. Singh, Vinod Singh Yadav, and V. Trivedi, "Experimental and numerical analysis of slurry pot

testerby response surface methodology (rsm) and computational fluid dynamics (cfd)," *Evergreen*, **10** (*2*) 931–941 (2023). doi:10.5109/6792888.

82) A. Jones, "Design Space Exploration and Optimization Using Modern Ship Design Tools," 2014. doi:10.21236/ADA609436.

83) W. Seok, G.H. Kim, J. Seo, and S.H. Rhee, "Application of the design of experiments and computational fluid dynamics to bow design improvement," *Journal of Marine Science and Engineering*, **7** (*7*) 226 (2019). doi:10.3390/jmse7070226.

84) N. Papanikolaou, and K. Anyfantis, "Construction of surrogate models for predicting the buckling strength of stiffened panels through doe and rsm methods," *Engineering Computations*, **39** (*4*) 1374–1406 (2022). doi:10.1108/EC-03-2021-0176.

85) ITTC, "Uncertainty analysis in cfd verification and validation, methodology and procedures," *Recommended Procedures and Guidelines*, **7.5-03-01-** (*Rev. 04*) (2021).

86) L.S. Lasdon, A.D. Waren, A. Jain, and M. Ratner, "Design and testing of a generalized reduced gradient code for nonlinear programming," *ACM Transactions on Mathematical Software (TOMS)*, **4** (*1*) 34–50 (1978). doi:10.1145/355769.355773.

87) Vikash Kumar Agrawal, and H.P. Khairnar, "Experimental & analytical investigation for optimization of disc brake heat dissipation using cfd," *Evergreen*, **9** (*4*) 1076–1089 (2022). doi:10.5109/6625720.

88) D.J. Taunton, D.A. Hudson, and R.A. Shenoi, "Characteristics of a series of high speed hard chine planing hulls - part 1: performance in calm water," *Transactions of the Royal Institution of Naval Architects Part B: International Journal of Small Craft Technology*, **152** 55–75 (2010). doi:10.3940/rina.ijsct.2010.b2.96.

89) J.H. Ferziger, and M. Perić, "Computational Methods for Fluid Dynamics," 2002. doi:10.1007/978-3-642-56026-2.

90) C.. Hirt, and B.. Nichols, "Volume of fluid (vof) method for the dynamics of free boundaries," *Journal of Computational Physics*, **39** (*1*) 201–225 (1981). doi:10.1016/0021-9991(81)90145-5.

91) F.R. Menter, "Two-equation eddy-viscosity turbulence models for engineering applications," *AIAA Journal*, **32** (*8*) 1598–1605 (1994). doi:10.2514/3.12149.

92) ITTC, "ITTC – recommended procedures and guidelines - practical guidelines for ship cfd applications. 7.5-03-02-03 (revision 01)," *ITTC – Recommended Procedures and Guidelines*, (2014).

93) Dandun Mahesa Prabowoputra, Aditya Rio Prabowo, I. Yaningsih, Dominicus Danardono Dwi Prija Tjahjana, Fajar Budi Laksono, R. Adiputra, and H. Suryanto, "Effect of blade angle and number on the performance of bánki hydro-turbines: assessment using cfd and fda approaches," *Evergreen*, **10** (*1*) 519–530 (2023). doi:10.5109/6782156.

94) M.M. Doustdar, and H. Kazemi, "Effects of fixed and dynamic mesh methods on simulation of stepped planing craft," *Journal of Ocean Engineering and Science*, **4** (*1*) 33–48 (2019). doi:10.1016/j.joes.2018.12.005.

95) S. Kaushik, V. Uniyal, Ajay Kumar Verma, Abhishek Kumar Jha, S. Joshi, M. Makhloga, Pankaj Singh Pargai, Saurabh Kumar Sharma, R. Kumar, and S. Pal, "Comparative experimental and cfd analysis of fluid flow attributes in mini channel with hybrid cuo+zno+h_2o nano fluid and (h_2o) base fluid," *Evergreen*, **10** (*1*) 182–195 (2023). doi:10.5109/6781069.

96) K. Hinkelmann, "Design and Analysis of Experiments," John Wiley & Sons, Inc., Hoboken, NJ, USA, 2012. doi:10.1002/9781118147634.

97) L.F. Richardson, "The approximate arithmetical solution by finite differences of physical problems involving differential equations, with an application to the stresses in a masonry dam," *Philosophical Transactions of the Royal Society A: Mathematical, Physical, and Engineering Sciences*, **210** (*459–470*) 307–357 (1911). doi:10.1098/rsta.1911.0009.

98) I.B. Celik, U. Ghia, P.J. Roache, C.J. Freitas, H. Coleman, and P.. Raad, "Procedure for estimation and reporting of uncertainty due to discretization in cfd applications," *Journal of Fluids Engineering*, **130** (*7*) 078001 (2008). doi:10.1115/1.2960953.

99) D. Savitsky, "Hydrodynamic design of planing hulls," *Marine Technology and SNAME News*, **1** (*04*) 71–95 (1964). doi:10.5957/mt1.1964.1.4.71.

100) ITTC, "Uncertainty analysis in cfd verification and validation methodology and procedures," *Recommended Procedures and Guidelines*, **7.5-03-01-** (2008).